Article

Rh2(II,III) Catalysts with Chelating Carboxylate and Carboxamidate Supports: Electronic Structure and Nitrene Transfer Reactivity

Adrián Varela-Álvarez, Tzuhsiung Yang, Heather Jennings, Katherine P. Kornecki, Samantha N. MacMillan, Kyle M. Lancaster, James Booker Christianson Mack, J. Du Bois, John F. Berry, and Djamaladdin G Musaev

J. Am. Chem. Soc., **Just Accepted Manuscript** • DOI: 10.1021/jacs.5b12790 • Publication Date (Web): 28 Jan 2016

Rh_2(II,III) Catalysts with Chelating Carboxylate and Carboxamidate Supports: Electronic Structure and Nitrene Transfer Reactivity

Adrián Varela-Álvarez,[a,†] Tzuhsiung Yang,[b,†] Heather Jennings,[b] Katherine P. Kornecki,[b] Samantha N. Macmillan,[c] Kyle M. Lancaster,[c] J. B. C. Mack,[d] J. Du Bois,[d] John F. Berry,[b,*] and Djamaladdin G. Musaev[a,*]

a) The Cherry L. Emerson Center for Scientific Computation, 1515 Dickey Dr., Emory University, Atlanta, GA 30322

b) Department of Chemistry, University of Wisconsin – Madison, 1101 University Ave. Madison, WI 53706

c) Department of Chemistry and Chemical Biology, Cornell University, Ithaca, NY 14853

d) Department of Chemistry, Stanford University, Stanford, CA 94305

Email: berry@chem.wisc.edu, dmusaev@emory.edu

†These authors have contributed equally to this work

Abstract

Dirhodium-catalyzed C–H amination is hypothesized to proceed *via* Rh_2-nitrene intermediates in either the Rh_2(II,II) or Rh_2(II,III) redox state. Herein, we report joint theoretical and experimental studies of the ground electronic state (GES), redox potentials, and C–H amination of $[Rh_2^{II,III}(O_2CCH_3)_4(L)_n]^+$ (**1_L**) (**L** = none, Cl^-, and H_2O), $[Rh_2(esp)_2]^+$ (**2**), and $Rh_2(espn)_2Cl$ (**3**) (esp = α,α,α',α'-tetramethyl-1,3-benzenedipropanoate and espn = α,α,α',α'-tetramethyl-1,3-benzenedipropanamidate). CASSCF calculations on **1_L** yield a wavefunction with two closely weighted configurations $(\delta^*)^2(\pi_1^*)^2(\pi_2^*)^1$ and $(\delta^*)^2(\pi_1^*)^1(\pi_2^*)^2$, consistent with reported EPR *g* values [*Chem. Phys. Lett.* **1986**, *130*, 20-23]. In contrast, EPR spectra of **2** show g values consistent with the DFT-computed $(\pi^*)^4(\delta^*)^1$ GES. EPR spectra and Cl K-edge XAS for **3** are consistent with a $(\pi^*)^4(\delta^*)^1$ GES, as supported by DFT. Nitrene intermediates **2N_L** and **3N_L** are also examined by DFT (the nitrene is an NSO_3R species). DFT calculations suggest a doublet GES for **2N_L** and a quartet GES for **3N_L**. CASSCF calculations describe the GES of **2N** as Rh_2(II,II) with a coordinated nitrene radical cation, $(\pi^*)^4(\delta^*)^2(\pi_{nitrene,1})^1(\pi_{nitrene,2})^0$. Conversely, the GES of **3N** is Rh_2(II,III) with a coordinated triplet nitrene, $(\pi^*)^4(\delta^*)^1(\pi_{nitrene,1})^1(\pi_{nitrene,2})^1$. Quartet transition states (^{4}TSs) are found to react *via* a stepwise radical mechanism, whereas ^{2}TSs are found to react *via* a concerted mechanism that is lower in energy as compared to ^{4}TSs for both **2N_L** and **3N_L**. The experimental (determined by intramolecular competition) and ^{2}TS-calculated kinetic isotopic effect (KIE) shows a KIE ~ 3 for both **2N** and **3N**, which is consistent with a concerted mechanism.

1. Introduction

C–H amination via nitrene transfer catalysis (NTC) has the potential to be a transformative method in synthetic organic chemistry.[1-5] Some of the leading catalysts for intra- and intermolecular C–H amination via NTC are coordination complexes with a Rh(II)–Rh(II) bond (Scheme 1), such as the Rh_2-tetracarboxylates and the $Rh_2(esp)_2$ (esp = α, α, α', α'-tetramethyl-1,3-benzenedipropanoate) catalyst bearing chelating dicarboxylate ligands, which operate best with sulfamate-derived nitrene species (NSO_3R).[6] Other catalysts such as silver,[7-11] iron,[12-17] manganese,[13, 18-20] ruthenium,[18, 21-23] copper,[24-30] and cobalt[31-34] complexes have been shown to perform C–H amination as well. The Rh_2(II,II) complexes were initially presumed to perform C–H amination via a nitrene interception/insertion mechanism, as shown in Scheme 1,[6, 35] in analogy to related carbene transfer reactions.[36] However, subsequently, Du Bois and Berry have independently shown the formation of mixed-valent Rh_2(II,III) species (including a Rh_2(II,III)-nitrene species proposed by Du Bois and Zare) under the highly oxidative NTC conditions, which are also believed to be active in NTC reactivity.[37-39]

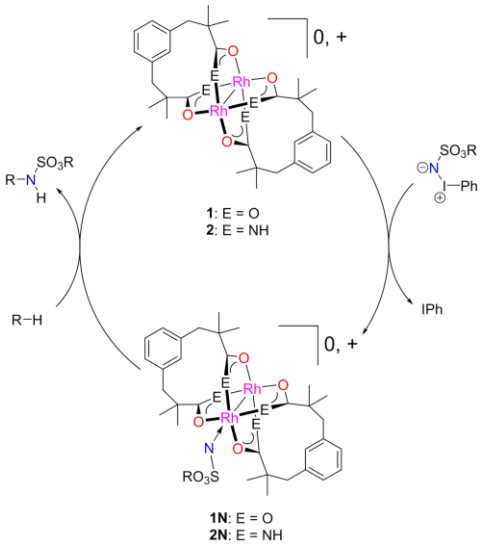

Scheme 1. NTC cycle for $Rh_2(esp)_2$ and $Rh_2(espn)_2Cl$.

Recently, the Berry group reported a new amidate-ligated Rh_2(II,III) catalyst, $Rh_2(espn)_2Cl$ (espn = α, α, α', α'-tetramethyl-1,3-benzenedipropanamidate), which is not only capable of performing intramolecular C–H amination, but it also has a long lifetime under NTC conditions, achieving turnover numbers higher than those of $Rh_2(esp)_2$ by a factor of three in head-to-head intramolecular competition experiments.[40] The longer lifetime of $Rh_2(espn)_2Cl$ during NTC as compared to $Rh_2(esp)_2$ may be attributed to the greater thermodynamic stability of the former complex. As has been well documented, amidate ligands not only bind more strongly to the Rh_2 core than do carboxylate ligands, but they also lower the potential required for oxidation of Rh_2(II,II) to the Rh_2(II,III) level.[41]

As compared to Rh_2(II,II) compounds, there are far fewer investigations of Rh_2(II,III) species. The most extensive electronic structure study of Rh_2(II,III) species, done by Norman and coworkers in 1979,[42] was very thorough but utilized methods that are now out of date and known to lead to inaccurate conclusions. The electronic structure of Rh_2(II,III) species is complex because of the existence of multiple low-lying electronic configurations, which could contribute to their total ground state wavefunction. Rh_2(II,II) complexes have a single Rh–Rh bond by virtue of the $(\sigma)^2(\pi)^4(\delta)^2(\delta^*)^2(\pi^*)^4$ electron configuration where all Rh–Rh bonding and antibonding orbitals are filled with the exception of the σ* antibonding orbital.[43] The π* and δ* orbitals located below the σ* orbital are very close in energy,[44] and thus,

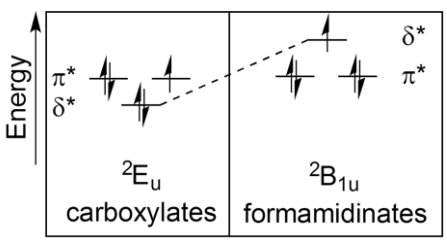

Chart 1. Possible ground states of Rh_2(II,III) compounds

upon oxidation of Rh_2(II,II) to Rh_2(II,III), it is *a priori* unclear whether a π* or δ* electron would be removed leading, in rigorous D_{4h} symmetry, to a ^2E_u or $^2B_{1u}$ ground electronic state (GES), respectively (Chart 1).

In principle, the ^2E_u and $^2B_{1u}$ states may be distinguished by EPR spectroscopy since the first-order spin-orbit coupling of the former state leads to the appearance of unusual EPR signals with *g* values widely different from the free electron value.[45] In this way, Kawamura and coworkers have shown that a range of Rh_2(II,III) carboxylate (O,O-donor) complexes have the ^2E_u ground state whereas Rh_2(II,III) compounds with N,N-donor ligands (e.g., formamidinates) have the $^2B_{1u}$ ground state.[46-49] An interesting question arises in considering Rh_2(II,III) complexes with amidate (N,O-donor) ligands: will these compounds have a ^2E_u ground state like the corresponding carboxylate compounds, or is the π-donation of the equatorial ligand field now strong enough that the δ* orbital is raised above the π* leading to a $^2B_{1u}$ ground state, like in the corresponding formamidinate compounds? An acetamidate-supported Rh_2(II,III) complex has been characterized by EPR spectroscopy in acetonitrile and DMSO solution, and was found to have *g* values, $g_\perp \sim 2.1$ and $g_\parallel \sim 1.9$, consistent with a single Kramer's doublet and therefore indicative of a $^2B_{1u}$-type $(\delta^*)^1$ ground state.[50]

Here we address the Rh_2(II,III) GES of $[Rh_2(OAc)_4(L)_n]^{m+}$, **1_(L)$_n$**, $[Rh_2(esp)_2(L)_n]^{m+}$, **2_(L)$_n$**, and $[Rh_2(espn)_2(L)_n]^{m+}$, **3_(L)$_n$**, [where L = none with m=1; L = H_2O, n=1 or 2 with m=1; L = Cl^-, n=1 with m =0; and L = Cl^-, n=2, with m = –1] species by EPR spectroscopy and, where applicable, Cl K-edge XAS, as well as by computational approaches including density functional theory (DFT) and *ab initio* state-averaged complete active space self-consistent field methods (SA-CASSCF), where necessary. Dynamic electronic correlation effects were included by utilizing multireference difference-dedicated configuration interaction theory with two degrees of freedom (MR-DDCI2). We also elucidate the impact of the nature of the GES of these Rh_2(II,III) complexes to the stability and reactivity of their proposed nitrene intermediates by investigating the intramolecular C–H amination catalyzed by **2_L** and **3_L** species. Although it is instructive to compare the GES of **2_L** and **3_L** with that of the simplified **1_L** species, the latter species are not included in the reactivity studies because NTC by **1_L** has not been established to utilize the Rh_2(II,III) oxidation state.

2. Results and Discussion.

2.A. Analysis of the Rh_2(II,III) Compounds.

2.A.1. Electronic Structure of Rh_2(II,III) Complexes. At first, we elucidate the GES of the Rh_2(II,III) complexes using the BP86 density functional method in conjunction with TZVP basis sets[51] for optimization of geometries. Reported DFT energies were derived from single-point B3LYP calculations on the BP86-optimized structures.[52-55] Redox potential calculations were performed using an established methodology.[56] MR-DDCI2:SA-CASSCF calculations were performed using various active spaces (see the Computational Methodology section for more details).

$[Rh_2(OAc)_4(L)_n]^{m+}$, 1_(L)$_n$, species. We start our discussion with Rh_2(II,III) tetra-acetate complexes $[Rh_2(OAc)_4]^+$, **1**, $[Rh_2(OAc)_4(H_2O)_2]^+$, **1_(H_2O)$_2$**, $[Rh_2(OAc)_4Cl]$, **1_Cl**, and $[Rh_2(OAc)_4(Cl)_2]^-$, **1_Cl$_2$.** Herein, we mostly focus on **1_(H_2O)$_2$** and **1_Cl$_2$** for which experimental data are available, but we also compare those to **1** to gauge the effect of axial

ligand coordination to the Rh_2(II,III) core. EPR spectra of $[Rh_2(OAc)_4(L)_n]^{m+}$ have been reported with L = H_2O, EtOH, and THF with n = 2 and m = 1, and Cl with n =2 and m = –1. The spectra are axial with $g_{\|}$ = 3.38 – 4.00 and $g_{\perp}$ = 0.6 – 1.5.[48] These unusual g values are described by Kawamura and coworkers as the result of a first-order spin-orbit interaction derived from the nearly-degenerate π* orbitals of the ^2E_u state, but computational support for these phenomenological assignments is lacking.[46-49]

To validate DFT methods against these experimental data, the GES and EPR parameters for the compounds **1**, **1_(H$_2$O)$_2$**, **1_Cl** and **1_(Cl)$_2$**, were calculated. These DFT calculations converged to the expected ^2E_u GES for all four complexes.[57] However, despite predicting the anticipated ^2E_u ground state, the DFT-calculated EPR g values are incompatible with the available experimental data: DFT predicts a markedly rhombic g tensor with abnormal values giving g_1, g_2, and g_3 of 7.36, 2.61, and 2.04 for **1**, 3.41, 2.32, and 2.07, for **1_(H$_2$O)$_2$**, 27.4, 2.43, and 2.13 for **1_Cl**, and 18.5, 2.77, and 2.14 for **1_Cl$_2$**, respectively, whereas the experimental spectra are axial with $g_{\|}$ ~ 4.00 and $g_{\perp}$ << 2.00 (see Table 1).

The aforementioned discrepancy between the experimental and DFT findings can be explained by the multi-determinant nature of the ^2E_u electronic state, where the energetic degeneracy of the π* orbitals presents an inherent problem for all single-determinant based methods, including DFT.[58] Indeed, a "proper" wavefunction of the ^2E_u electronic state should include, at least, the following two simplified determinants

$$\Psi(^2E_u) = \frac{1}{\sqrt{2}}[|(\pi_1^*)^2(\pi_2^*)^1| + |(\pi_1^*)^1(\pi_2^*)^2|] \qquad \text{eq. 1}$$

because the unpaired electron has an equal probability of being housed in either the π_1^* or the π_2^* orbital. In order to properly describe such a multi-determinant system allowing for an accurate prediction of g tensors of the complexes, the CASSCF approach is utilized.

The leading determinants of the SA-CASSCF wavefunctions with their weights are given in Table 2. For all **1_L** compounds, there are two leading determinants that contribute equally, or nearly equally, to their total wavefunctions. In all cases, these two leading determinants are those that differ in their π^*_1 and π^*_2 occupation, as anticipated from the above discussion. Thus, the CASSCF results are fully consistent with ^2E_u-derived ground states for these compounds.

The MR-DDCI2 method was used on the converged SA-CASSCF wavefunction to predict the g values of $[Rh_2(OAc)_4]^+$: an axial signal with $g_{\|}$ = 4.00 and $g_{\perp}$ = 0.05 is predicted. As seen in Table 1, where we provide all calculated and experimental g values for $[Rh_2(OAc)_4]^+$, $[Rh_2(OAc)_4(H_2O)_2]^+$, $Rh_2(OAc)_4Cl$ and $[Rh_2(OAc)_4Cl_2]^-$, the MR-DDCI2:SA-CASSCF-calculated EPR g values are in close agreement with the experimental values. These findings additionally support that all these species have a ^2E_u ground state containing a $(\pi^*)^3$ valence electron configuration.

*Thus, due to existence of the orbital degeneracy in **1_L**$^+$, the DFT approach is not the best method to calculate the lowest energy electronic states and related properties of these compounds.*

$[Rh_2(esp)_2L]^+$. To date, only one set of crystallographic data is available for a metastable Rh_2(II,III) complex bearing *esp* ligands, $[Rh_2(esp)_2Cl_2]^-$.[39] In this paper, we report optimized geometries of the species $[Rh_2(esp)_2]^+$, **2**, $[Rh_2(esp)_2(H_2O)]^+$, **2_H$_2$O**, and $Rh_2(esp)_2Cl$, **2_Cl**. In Table 3, we compare the optimized parameters of these species with the available crystallographic values. As seen from this table, the DFT approach describes the Rh–Rh and Rh–O_{av} distances well.

DFT calculations on **2** surprisingly predict a $^2B_{1u}$-derived GES with a $(\delta^*)^1$ electron configuration. Analysis shows that in this compound, like in the case of the $[Rh_2(OAc)_4]^+$ complexes, the δ* orbital has significant anti-bonding contributions from the O–C–O π* carboxylate (bridging) orbitals. However, unlike the case of $[Rh_2(OAc)_4]^+$ complexes, the δ* orbital of **2** also has a contribution from the *m*-phenylene moieties of the esp ligands, an apparent through-space interaction at 4.3 Å. This interaction slightly destabilizes the δ* orbital, and, consequently, makes the $^2B_{1u}$-type $(\delta^*)^1$ electronic state more favorable for $[Rh_2(esp)_2]^+$ compared to the $[Rh_2(OAc)_4]^+$ complexes.

To experimentally substantiate the computationally predicted $^2B_{1u}$-derived ground state with a $(\delta^*)^1$ orbital configuration of **2**, we turned our attention to spectroscopic studies. As shown previously, $Rh_2(esp)_2$ is not stable in the Rh_2(II,III) redox state, but in CH_2Cl_2 solution it can be oxidized coulometrically to the corresponding Rh_2(II,III) species **2**.[39] The coulometric oxidation was monitored by UV-vis spectroscopy, which showed near-isosbestic behavior indicative of oxidation to an isostructural product with the possibility of a partial transformation of the oxidized product via a chemical reaction. A sample of electrochemically generated **2** was frozen upon generation and analyzed by EPR spectroscopy. The EPR spectrum given in Figure 1 is surprising in two ways. First, the spectrum cannot be simulated by a single S = ½ species and therefore indicates that **2** actually contains *two* Rh_2(II,III) species that are similar in structure as evidenced by the similarity of their axially symmetric EPR signals. Second, the best-simulated EPR g values, $g_\perp$ = 2.124 and $g_\parallel$ = 1.928 for the first species, and $g_\perp$ = 2.255 and $g_\parallel$ = 1.893 for the second species, are indicative of a relatively simple S = ½ species with a single Kramers' doublet excluding the possibility of having a ground state with the $(\pi^*)^3$ orbital configuration for **2**. The observed g values instead fit well in the range of those observed for compounds with a ground state containing a $(\delta^*)^1$ orbital.[50] As for the reason that two EPR-active species are produced during coulometric oxidation of $[Rh_2(esp)_2]$, this is likely due to partial coordination of a solvent

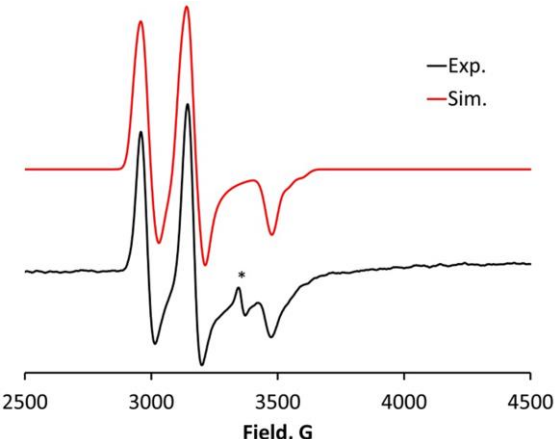

Figure 1. X-Band EPR spectrum measured at 10 K of an electrochemically oxidized solution of $Rh_2(esp)_2$. The spectrum is modeled with two axially symmetric subspecies present in a 1:1 ratio. Species 1: $g_\perp$ = 2.124, $g_\parallel$ = 1.928, $A_\perp$ = 95 MHz. Species 2: $g_\perp$ = 2.255, $g_\parallel$ = 1.893, $A_\perp$ = 93 MHz, $A_\parallel$ = 150 MHz. Instrument parameters: mw frequency = 9.3814 GHz, power = 0.6325 dB, attenuation = 25 dB, modulation frequency = 100 kHz, modulation amplitude = 4 G, receiver gain = 70 dB, time constant = 163.84 ms, conversion time = 10 ms.

or electrolyte species in the axial site of the Rh_2 molecule to generate Rh_2 species such as $Rh_2(esp)_2Cl$, which has been observed in a high-resolution mass spectrum,[35] and is consistent with the imperfect isosbestic behavior of the oxidation. Notably, the EPR parameters predicted by DFT for **2**, g_1 = 2.24, g_2 = 2.11, g_3 = 2.06, differ in symmetry but are close to the experimental values.

*Comparison of the DFT calculated electronic state and aforementioned EPR data clearly show that the utilized DFT approach provides an adequate description of the ground state wavefunction of **2** and its derivatives. Thus DFT can be used to further explore the chemistry of these species.*

$[Rh_2(espn)_2L]^+$, 3_L. Recently, Berry and coworkers have reported a new amidate-ligated catalyst, $Rh_2(espn)_2Cl$, **3_Cl**, which can form as any one of four possible isomers: the (*cis*-2,2)-, (4,0)-, (*trans*-2,2)-, and (3,1)-isomers. However, the synthesis of **3_Cl** results in two structural isomers (*cis*-2,2)-**(3_Cl)** and (4,0)-**(3_Cl)**, with the *cis*-2,2 isomer favored in a 4:1 ratio.[40] At low concentrations, **3_Cl** dissociates Cl^- in CH_2Cl_2 to form $[Rh_2(espn)_2]^+$, **3**, and it was possible to assign electrochemical features to both the Cl-bound and unbound species.[40]

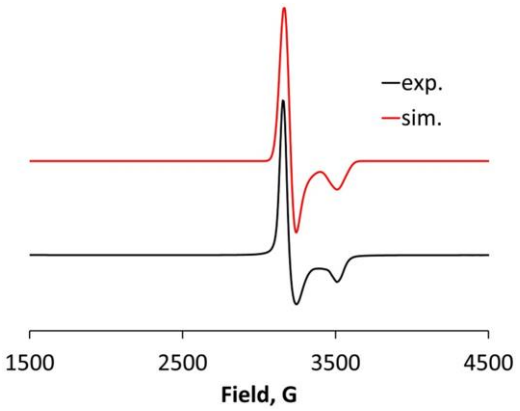

Figure 2. X-Band EPR spectrum measured at 10 K of 4,0-$Rh_2(espn)_2Cl$. The spectrum is modeled with $g_\perp$ = 2.105, $g_\parallel$ = 1.905, and $A_\parallel$ = 135 MHz. Instrument parameters: mw frequency = 9.3792 GHz, power = 0.6385 mW, attenuation = 25.0 dB, modulation frequency = 100 kHz, modulation amplitude = 4 G, receiver gain = 30 dB, time constant = 327.68 ms, conversion time = 10.0 ms.

We report here experimental EPR and XAS measurements aimed at elucidating the nature of the ground state of **3**. EPR data on the $[Rh_2(espn)_2L]^+$ complexes in solution are consistent with an S = 1/2 ground state for these species. Indeed, the spectra of these compounds can be straightforwardly simulated by near-axial S = 1/2 signals showing ^{103}Rh hyperfine splitting of the $g_\parallel$ signal. The best simulations of these spectra yield the following parameters: $g_\perp$ = 2.11, $g_\parallel$ = 1.927, $A_\parallel$ = 90 MHz for (*cis*-2,2)-**(3_Cl)** and $g_\perp$ = 2.105, $g_\parallel$ = 1.905, $A_\parallel$ = 135 MHz for (4,0)-**(3_Cl)** (see Figure 2). Our results compare favorably with those reported by Kadish, Bear, and coworkers on Rh_2(II,III) acetamidate analogs, which have $g_\perp$ = 2.11-2.13, $g_\parallel$ = 1.89-1.92, and $A_\parallel$ = 79-90 MHz.[50] These data support the assignment of the GES with a $(\delta^*)^1$ configuration for **3**.

Another spectroscopic method that has not yet been used with metal-metal bonded compounds but in principle can distinguish between the $(\pi^*)^3$ and $(\delta^*)^1$ states in $[Rh_2(II,III)]$-Cl complexes is Cl K-edge X-ray absorption spectroscopy (XAS). Cl K pre-edge transitions may be formally assigned as Cl 1s → "φ" where φ represents a molecular orbital of the form [α(Rh *4*d) + $\sqrt{1-\alpha^2}$ (Cl 3p)]. Here, the presence of Cl 3p character in partially unoccupied valence orbitals is required for non-zero Cl K pre-edge intensity. From symmetry considerations, Cl character can be mixed into σ- or π-type orbitals in a linear Rh–Rh–Cl structure, but cannot be mixed into δ-symmetry orbitals. Thus, a $(\pi^*)^3$ compound should display a pre-edge feature below the main

σ* transition corresponding to the partially filled Rh_2 π* level, and a $(\delta^*)^1$ compound should not. Thus, in the case of the anticipated $(\delta^*)^1$ ground state of **3_Cl** we expect to observe a Cl 1s → σ* pre-edge transition, whereas with a $(\pi^*)^3$ ground state there would be an additional, resolvable lower energy transition: Cl 1s → π*. The Cl pre-edge region for **3_Cl** is shown along with its corresponding second-derivative plot and least-squares fit in Figure 3. The pre-edge region comprises a single peak at 2822.1 eV. The presence of a single peak is consistent with a GES having a Rh–Rh δ* SOMO.

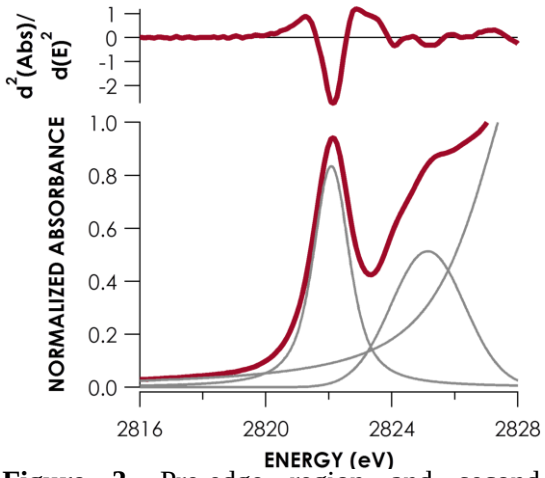

Figure 3. Pre-edge region and second derivative plot of (*cis*-2,2)-$Rh_2(espn)_2Cl$ Cl K-edge XAS. Pseudo-Voigt peaks are shown in gray.

To support these experimental results, we have computationally investigated the (*cis*-2,2) and (4,0) isomers of $[Rh_2(espn)_2]^+$, **3**, $[Rh_2(espn)_2(H_2O)]^+$, **3_H₂O**, and $Rh_2(espn)_2Cl$, **3_Cl** species. Their calculated and experimental geometries at the ground doublet electronic states (with the unpaired electron in the Rh–Rh δ* orbital) are given in Table 4. One should mention that the (4,0)-(**3_L)** species could have two isomers, which differ by coordination of the L ligand to the Rh_2-center surrounded by either four N-centers or four O-centers. Below, we call these isomers as $(4,0)_N$ and $(4,0)_O$, respectively. In general, the $(4,0)_N$ isomer is found to be energetically a few kJ/mol more favorable than the $(4,0)_O$ isomer for both doublet and quartet state species. The energy difference between these isomers is slightly larger for L = Cl than H_2O. For simplicity, below we discuss only the energetically more stable $(4,0)_N$ isomers of **3_H₂O** and **3_Cl** species, but we include all energy and geometry results for the less stable $(4,0)_O$ isomers of **3_H₂O** and **3_Cl** in the supporting material.

As seen from Table 4, in general, the calculated geometries of the doublet *S* = 1/2 GESs of **3, 3_H₂O** and **3_Cl** with the unpaired electron in the Rh–Rh δ* orbital match closely their experimental values. One major disagreement between the calculated and experimental structures occurs for (*cis*-2,2)-**(3_Cl)**: the experimental structure of this species is polymeric, with Cl^- ions bridging an infinite chain of Rh_2 species. In contrast, its calculated structure is molecular with a monodentate Cl^- ligand. As a result, the Rh–Cl bond distance is severely underestimated in the calculation, which, in turn, leads to an overestimation of the Rh–Rh bond distance. Since the Cl-bridged structure is a feature only of the solid-state packing of this compound and is likely absent in homogeneous solution, the calculated structure is presumably a more accurate model for the compound in solution during catalysis.

After elucidating the electronic and geometric structures of the aforementioned Rh_2(II,III) species, we are well positioned to discuss their redox potentials, which are vital for understanding the stability and reactivity of these species. Based on the above-presented comparison of DFT, and experimental data, one may confidently use DFT methods to calculate redox potentials and provide insight into the proclivity for axial ligand binding of the Rh_2(II,III) species **2_L** and **3_L**. We excluded **1_L** species from reactivity studies due to the facts that: (a)

NTC by **1_L** has not been established to utilize the Rh_2(II,III) oxidation state, and (b) the GES of **1** is multi-configurational and, therefore, may not be accurately described by the DFT approach.

2.A.2. Energy Landscape: Redox Potentials and Axial Ligand Effects. For $[Rh_2(esp)_2]^+$, **2**, experiments showed that the $\mathbf{2}^{0/+}$ redox potential is at 0.80 V vs Fc/Fc^+.[39, 59] DFT predicts a value of 0.78 V, which in excellent agreement with the experimental value (see Scheme 2). The calculated $[\mathbf{2\_Cl}]^{0/-}$ redox potential is –0.72 V vs Fc/Fc^+. Since previous experiments showed that **2** strongly binds Cl^- ions,[35] we also calculated the impact of a second Cl^- ligand binding to $[Rh_2(esp)_2]^+$, **2**. It was found that the binding of two Cl^- ligands to **2** greatly lowers the Rh_2(II,II)/Rh_2(II,III) (in short $Rh_2^{4+/5+}$) redox potential by 2.27 V. These findings show that increasing the concentration of chloride (or any other anionic potential axial ligand for that matter) in reaction mixture, could strongly favor catalysis in the Rh_2(II,III) regime, though if the concentrations are too high catalysis could be hindered by blocking of both axial sites.

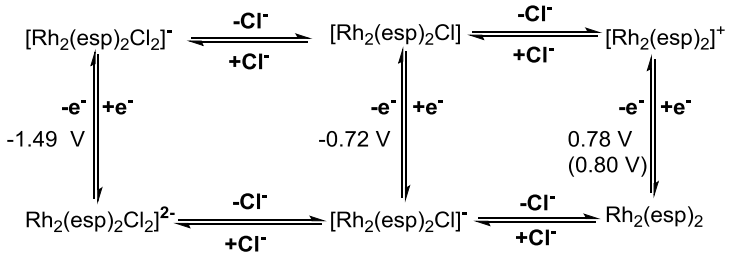

Scheme 2. Energy landscape of compounds **2, 2_Cl** and **2_Cl$_2$**. DFT-calculated and experimental redox potentials are given without and with parentheses, respectively.

As mentioned above, experiments showed that complex **3_Cl** could have several isomers among which the (*cis*-2,2) and (4,0) isomers are experimentally observed, with the *cis*-2,2 isomer favored in a 4:1 ratio.[40] Consistent with this finding, DFT calculations predict the (*cis*-2,2)_(**3_Cl**) isomer to be lower in energy than the (4,0) isomer by 12.1 kJ/mol (see Scheme 3). Dissociation of the axial chloride ligand leads to the active cationic catalyst, $[Rh_2(espn)_2]^+$, the (*cis*-2,2)-**3** isomer of which is higher in energy by 15.5 kJ/mol than its (4,0)-**3** isomer. The four nitrogen atoms bound to the high oxidation state Rh^{III} center in the (4,0) isomer, therefore, appear to provide greater stabilization to the Rh atom than two nitrogen and two oxygen atoms as in the (2,2) isomer.

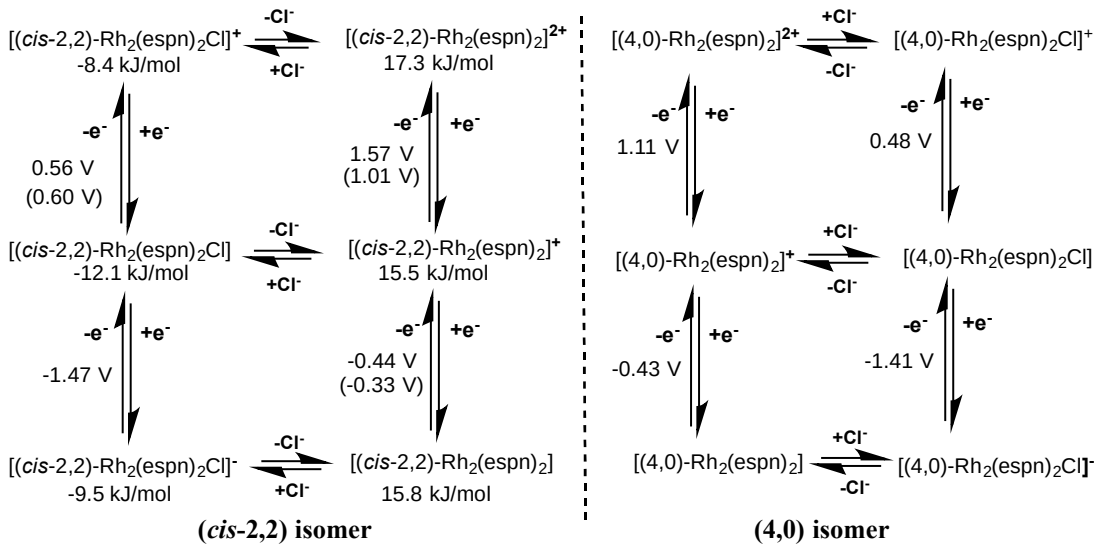

Scheme 3. Energy landscape of compounds (*cis*-2,2)-**3** and (*cis*-2,2)-(**3_Cl)**, as well as (4,0)-**3** and (4,0)-(**3_Cl)**. DFT-calculated and experimental redox potentials (listed relative to the Fc/Fc^+ couple) are given without and with parentheses, respectively. Presented relative energies (in kJ/mol) are listed relative to the corresponding (4,0)-isomers.

Cyclic voltammetry experiments were performed for (*cis*-2,2)-**3** which showed two reversible waves corresponding to $[Rh_2(espn)_2]^{0/+}$ at –0.33 V and $[Rh_2(espn)_2]^{+/2+}$ at 1.01 V. A third quasi-reversible peak was observed at 0.60 V which was assigned to the chloride bound $[Rh_2(espn)_2Cl]^{0/+}$ redox couple.[40] For (*cis*-2,2)-**3**, DFT calculations predicted the $[Rh_2(espn)_2]^{0/+}$ couple at –0.44 V and the $[Rh_2(espn)_2]^{+/2+}$ couple at 1.57 V. The $[Rh_2(espn)_2Cl]^{0/+}$ couple is predicted at 0.56 V. Here the agreement between calculated and experimentally measured redox potentials is superb, providing excellent support for the assignments of these waves as well as validation for the DFT methods used (see Computational procedure for more details). The one exception is the redox couple involving the dicationic species $[(cis\text{-}2,2)\text{-}Rh_2(espn)_2]^{2+}$, where the discrepancy is likely the result of stronger solvation effects on the energy of the dication. For the (4,0) isomer of **3**, the $[Rh_2(espn)_2]^{0/+}$ couple was predicted at –0.43 V and the $[Rh_2(espn)_2]^{+/2+}$ couple at 1.11 V. The $[Rh_2(espn)_2Cl]^{0/+}$ couple was predicted at 0.48 V. All of the calculated and measured redox potentials are summarized in Scheme 3.

This analysis of Rh_2 electronic states and redox potentials now positions us to investigate catalytically relevant intermediates of the mixed-valent Rh_2(II,III) complexes **2_L** and **3_L**, and study intimate mechanistic details of C–H amination catalyzed by these systems, where **L** = none, **H_2O** and **Cl**.

2.B. Rh_2(II,III) Nitrene Complexes and Mechanism of the intramolecular C–H amination.

2.B.1. Electronic Structure of the Rh_2(II,III)-Nitrene Intermediates. As mentioned above (see Scheme 1), one of the most important intermediates of both intra- and intermolecular C–H amination by the mixed-valent Rh_2(II,III) species under oxidative NTC conditions is the transient Rh_2(II,III)-nitrene complex. Since isolation and characterization of these transient complexes has, to date, not been possible, DFT and CASSCF computations, validated above, appear to be

the most valuable tool to study the electronic and geometric structures, as well as reactivity of these species.

DFT calculations were used to optimize structures of the **2N_L** and **3N_L** nitrene complexes of the species **2_L** and **3_L**, respectively, as described in more detail in the Computational Methodology section. The results are given in Tables 5 and 6. In all structures, the Rh–Rh distances of 2.39 – 2.48 Å are not much changed from those of **2_L** and **3_L**. Importantly, the addition of an **L** ligand has little effect on the Rh–Rh distances but elongates the Rh–N_{ax} bond distance, more notably in the doublet state for **2N_L**, but the effect is seen in both spin states of **3N_L** compounds. Interestingly, in doublet **2N**, the C^1–H^1 bond of the nitrene fragment interacts with the N-center and, already, is partly activated with C^1–H^1, N–H^1, and Rh–N distances of 1.15, 1.65, and 1.92 Å, respectively (see also Figure 8).

In all **2N_L** and **3N_L** complexes, the doublet and quartet states are predicted by DFT to be quite close in energy. For the **2N_L** series, the doublet states are predicted to be lowest in energy by 9.6 and 13.8 kJ/mol with L = none and Cl^-, respectively. The aquo complex is predicted to have the quartet state lower in energy by a (practically negligible) 4.6 kJ/mol. For the **3N_L** compounds, the quartet states are all lower in energy, presumably due to the higher destabilization of the δ* orbital by the more electron-donating equatorial N-donors. The energy differences to the doublet states range from 9 – 15 kJ/mol for the *cis*-(2,2) isomers, and from 8 – 11 kJ/mol for the (4,0) isomers.

In general, the sulfamate-derived nitrene can utilize its σ and two π orbitals to form bonds with the σ- and π-symmetry orbitals of the Rh_2(II,III) core, similar to those previously described for Rh_2-carbene and Ru_2-nitride compounds.[60-68] The important frontier orbitals of the nitrene complexes are the Rh_2-centered δ* orbital, two three-center Rh–Rh–N π* orbitals, and the three-center Rh–Rh–N σ* orbital (see Chart 2). The δ* and π* orbitals are expected to be close in energy, as is well-known in other Rh_2 and Ru_2 systems with a similar electron count.[5, 63-67, 69] However, the π* orbitals are expected to differ in energy since one of these two orbitals, denoted π*′, is also involved in the N–S bond of the bent nitrene unit. Thus, the similar energies of the doublet or quartet states for the nitrene complexes are derived from configurations with differing population of the δ* and π* levels. The configuration of the quartet state is $(\delta^*)^1(\pi^{*\prime})^1(\pi^{*\prime\prime})^1$, but there are several possible doublet configurations to consider. Importantly, the major acceptor orbitals for electrophilic reactivity are the Rh–Rh–N π* orbitals, which are heavily polarized towards the N atoms.

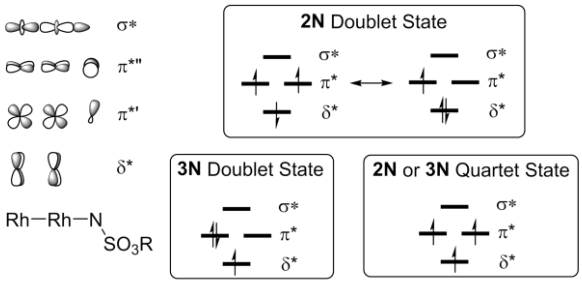

Chart 2. Molecular orbital ordering of [Rh–Rh]–NSO_3R compounds, with the highlighted electron configurations of the doublet and quartet states. Only the major electron configuration is shown in each case. Two π* orbitals are shown as degenerate only for simplicity.

Due to the several possible electron configurations for the doublet state, we may expect the doublet states of **2N** and **3N** to be multi-configurational, with three valence electrons in the near-degenerate δ*, π*′, and π*″ orbitals. To gauge the importance of this effect, and to extract a useful description of the bonding in these compounds, both DFT and CASSCF calculations on

2N and **3N** complexes were performed with the simplifying truncation of CH_3 for the organic substituent on the nitrene group (labeled **2N′** and **3N′**). Two distinct DFT models for doublet-state **2N′** were considered containing either a singlet or triplet nitrene coordinated to the Rh_2 unit. As shown in Table S1, these two configurations are nearly isoenergetic but have drastically different spin distributions. For reference, the DFT frontier orbitals of the singlet nitrene configuration are shown in Figure S1. A similar situation arises when the doublet state of **3N′** is examined by DFT methods (Table S1). Two drastically differing doublet states are found to be different by only ~ 8 kJ/mol. Due to the ambiguity in the DFT-calculated electronic structure, further analysis of the bonding in these intermediates was made at the CASSCF level.

The CASSCF electronic configurations of **2N′** and **3N′** and their corresponding weights are given in Tables 7 and 8. The natural orbitals of the multiconfigurational wavefunction are shown in Figures 4 and 5. Both quartet states are quite similar, with the anticipated $(\delta^*)^1(\pi^{*\prime})^1(\pi^{*\prime\prime})^1$ configurations and spin delocalized throughout the Rh–Rh–N unit. The doublet states of **2N′** and **3N′** are electronically distinct. As seen in Figure 4, there is significant mixing of the orbitals of δ* and π*″ symmetry in **2N′** leading to some fluidity in its electronic structure. We may describe the electronic structure as a resonance hybrid between a $(\delta^*)^2(\pi^{*\prime})^1(\pi^{*\prime\prime})^0$ configuration and an antiferromagnetic $(\delta^*)^d(\pi^{*\prime})^u(\pi^{*\prime\prime})^u$ configuration (here d and u denote spin-down and spin-up, respectively). The former configuration may be described in valence bond terms as having a Rh_2(II,II) unit with a coordinated nitrene radical cation, while the latter configuration indicates a Rh_2(II,III) species that is antiferromagnetically coupled to a triplet nitrene group. The view that both of these configurations contribute to the ground state is supported by the Mulliken spin populations showing very little (but negative) spin on the Rh centers and 1.05 spin on the nitrene N atom. It is remarkable that the calculations support partial oxidation of the nitrene moiety, itself a strong oxidant, by the $Rh_2(esp)_2^+$ core. This result is, however, in agreement with the high $Rh_2(esp)_2^{0/+}$ redox potential, but since we have shown the redox potentials to drop considerably upon chloride binding, it is likely that the electronic structure will change significantly as a function of the axial ligands.

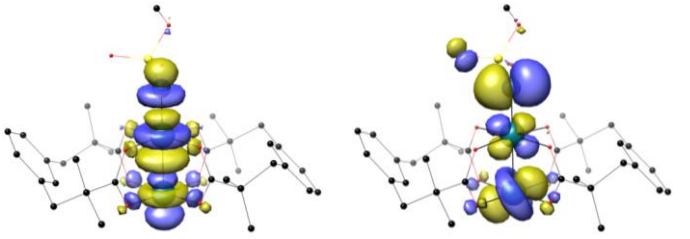

σ* [0.112562] π"*-δ* [0.807063]

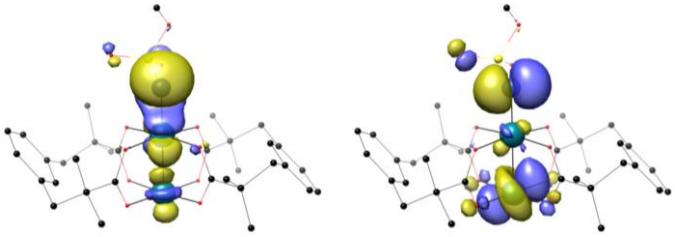

π'* [1.028932] π"*+δ* [1.227204]

Figure 4. Frontier orbitals of the natural orbitals of doublet **2N'** from CASSCF. Occupation numbers are shown in bracket.

As expected from the greater stabilization of higher oxidation states by espn, the major configuration of **3N′**, $(\delta^*)^1(\pi'^*)^2(\pi''^*)^0$, is best described as consisting of an Rh_2(II,III) unit coordinated by a singlet nitrene species (see the orbitals and occupation numbers given in Figure 5. Here, the spin population is clearly localized on the Rh_2 unit. In each case, there are other minor configurations contributing up to 26% of the wavefunction that are due to double- and single-exitations from the main configuration.

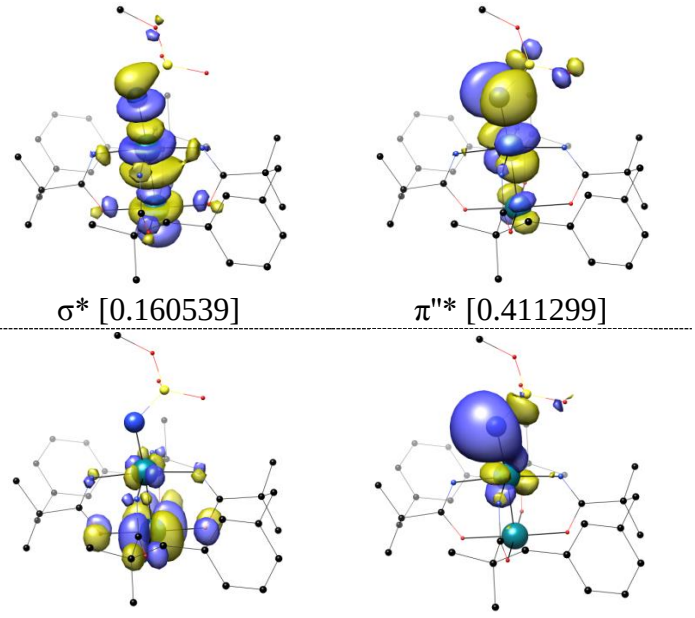

σ* [0.160539] π"* [0.411299]

δ* [1.031735] π'* [1.997225]

Figure 5. Frontier orbitals of the natural orbitals of doublet **3N'** from CASSCF. Occupation numbers are shown in brackets.

It is instructive at this juncture to compare the electronic structure of **2N′** and **3N′** to Co porphyrin complexes, which have been shown to undergo metal-centered oxidation upon the binding of alkyl sulfamate nitrenes to give Co(III)(Por)($NSO_3R^{\bullet-}$) species.[70] As shown in Figure 6, the electronic structures of both **2N′** and **3N′** are quite different from that of the Co species. One reason for this difference can be understood from the redox potentials of the respective

catalysts. **2** exhibits a $Rh_2^{4+/5+}$ couple at 0.78 V *vs* Cp_2Fe and **3** exhibits a $Rh_2^{5+/6+}$ couple at 1.57 V *vs* Cp_2Fe in CH_2Cl_2 (vide supra). In contrast, Co(TPP) (TPP = tetraphenylporphyrin) has been shown to exhibit three oxidation waves at 0.24, 0.45, and 0.61 V *vs* Cp_2Fe in CH_2Cl_2, corresponding to one metal-centered and two ring-centered oxidations, respectively.[71] Thus, Co(II) is able to reduce the nitrene group to a radical anion while neither the $Rh_2(esp)_2^+$ core nor the $Rh_2(espn)_2^+$ core are reducing. In fact, $Rh_2(esp)_2^+$ is highly oxidizing and there is a contribution to the GES of **2N′** from a Rh_2(II,II) species bearing a nitrene radical cation. In contrast, the $Rh_2(espn)_2^+$ core is content in the Rh_2(II,III) oxidation state and supports a bound singlet nitrene. In addition to the difference in the redox potentials, there is also a difference in the mechanism of C–H amination between the Co(Por) system, which has been proposed to proceed via stepwise mechanism,[72] whereas we propose here that both Rh_2 systems operate via a concerted mechanism (vide infra).

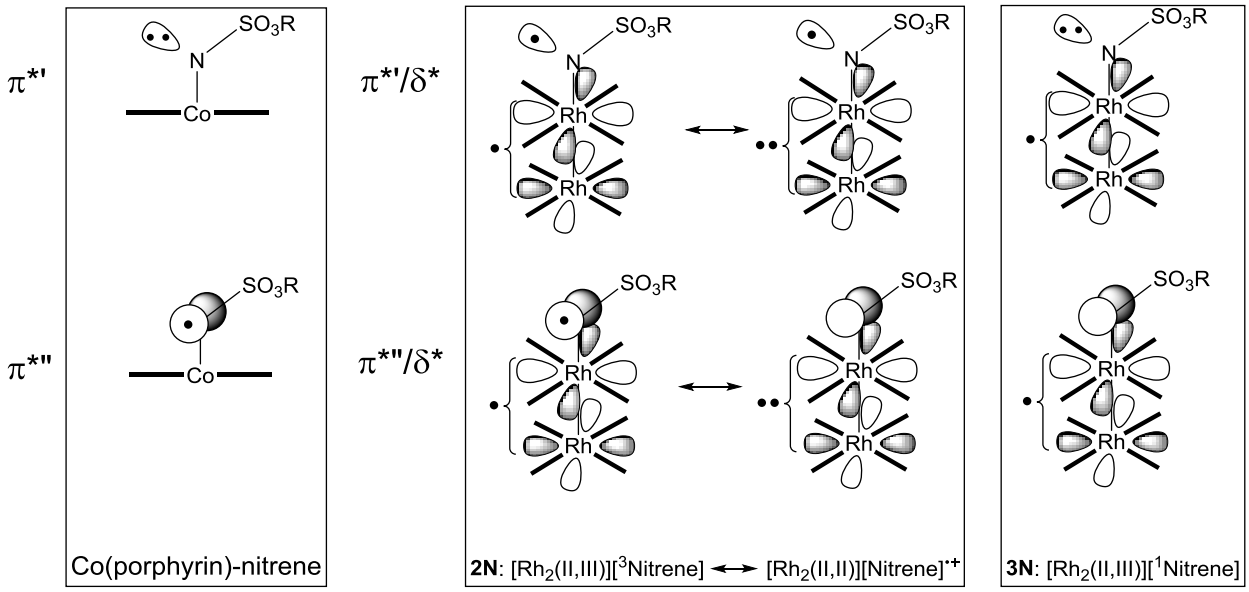

Figure 6. Comparison of the electronic structure of Co-porphyrin-nitrene(radical) species (left) with **2N′** (center) and **3N′** (right). Here, the two π-symmetry orbitals are shown separately and localized on N, and in the Rh_2 cases the δ* electrons are also shown.

We further investigated, at the DFT level, both doublet and quartet potential energy surfaces for C–H amination via the nitrene complexes $\{Rh_2(esp)_2(L)[NSO_3(CH_2)_3Ph]\}^{n+}$, **2N_L**, and $\{Rh_2(espn)_2(L)[NSO_3(CH_2)_3Ph]\}^{n+}$, **3N_L** keeping in mind the caveat that the doublet states are multi-configurational and that the DFT description of their electronic structure does not explicitly take this complexity into account. A full analysis of the potential energy surfaces at the CASSCF level cannot be performed because it is prohibitively expensive.

2.B.2. Mechanistic details of intramolecular C–H amination via 2N_L and 3N_L nitrene complexes. There are two limiting mechanisms for nitrenoid C–H amination that should be considered: concerted (**C**) and stepwise (**S**) insertion of the nitrene into a substrate C–H bond (Scheme 4). In the **C** mechanism, there is a single transition state leading to C^1–N bond formation, C^1–H^1 bond cleavage, and N–H^1 bond formation. The **S** mechanism starts by hydrogen atom (H^1) transfer (HAT) to produce a protonated nitrene radical anion and a benzylic

radical followed by radical recombination to yield the products. Unpaired spin density on the nitrene N atom is often naively suggested to support HAT in an **S** mechanism, but there are strong kinetic and thermodynamic arguments against such generalizations.[73] Below, we develop an electronic structure-based approach to understand the differences between a **C** and **S** mechanism.

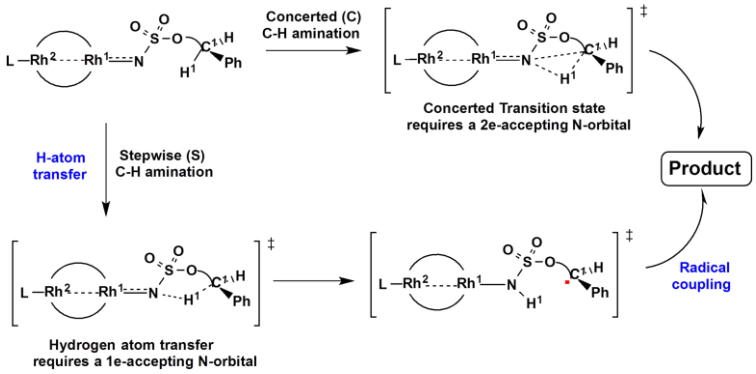

Scheme 4. Schematic presentation of the concerted (**C)** and stepwise (**S)** mechanisms of intramolecular nitrene insertion into a substrate C–H bond in the **2N_L** and **3N_L** nitrene complexes.

If we consider the orbital requirements for a **C** mechanism, the three-membered N–C^1–H^1 ring of the transition state will require one orbital from each of the nuclei involved: a N p-orbital (or sp^x hybrid), a C^1 p- or sp^x-hybrid orbital, and a H^1 1s-orbital. The stabilization of a three-membered ring with three orbitals requires the presence of two electrons, to form a 3c/2e bond. These two electrons obviously originate from the C^1–H^1 bond of the substrate. *Thus, this mechanism requires an empty (but energetically accessible) N-centered orbital that can accept two electrons from the C–H bond.*

The electronic requirements of the **S** mechanism are different. This mechanism relies on an HAT step, and requires the N atom to accept a single electron. Therefore, *this mechanism requires either an empty or half-filled N-centered orbital capable to accept the incoming H^1 atom with one unpaired electron.*

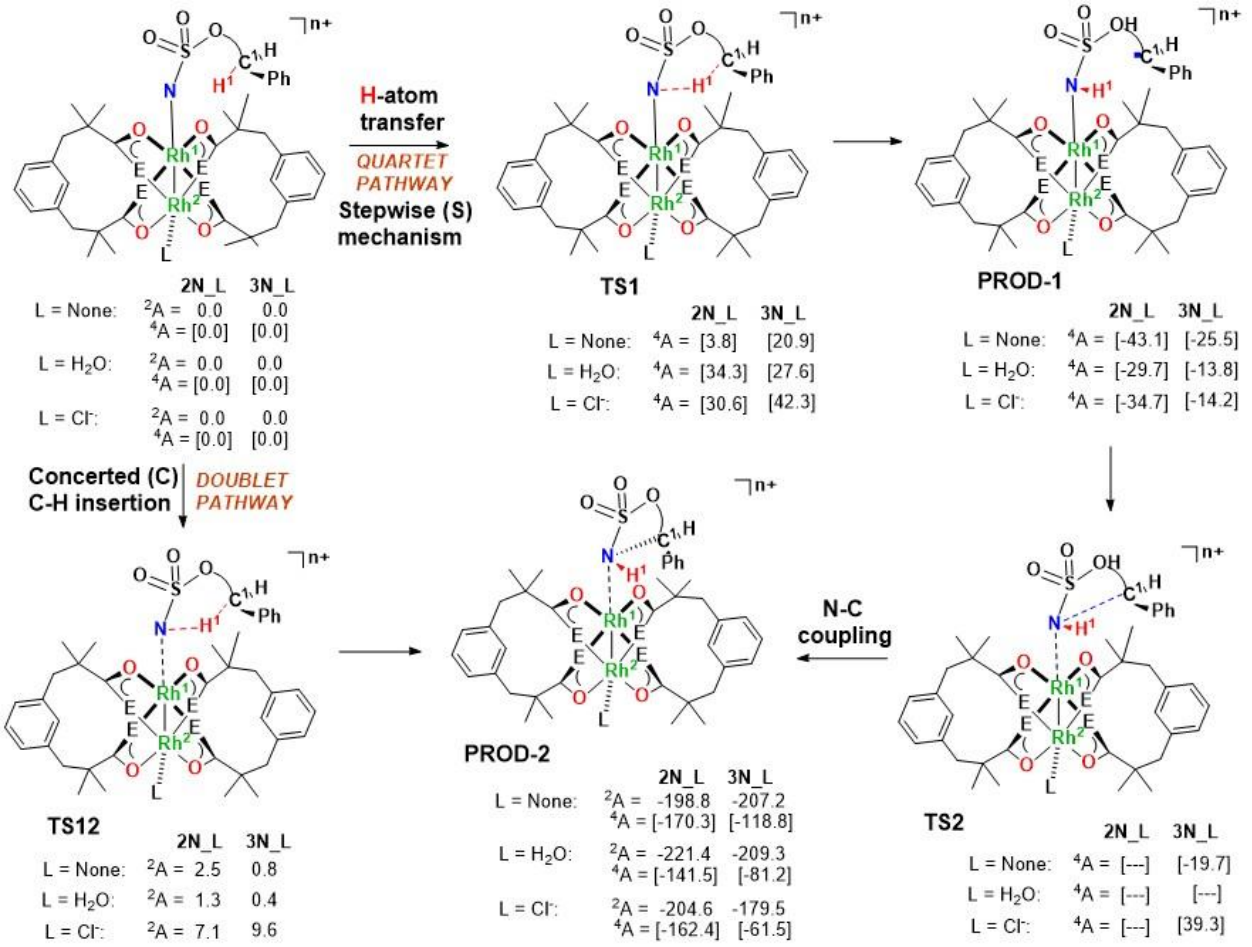

Figure 7. Schematic representation of the calculated reactants, intermediates, transition states and products, alone with their relative energies (relative to the corresponding reactants, in kJ/mol), of the intramolecular C–H amination in the **2N_L** and **3N_L** nitrene complexes.

Based on the aforementioned discussion, it can be expected that intramolecular C–H amination in the doublet state nitrene complexes with an empty and easily accessible Rh–Rh–N π* orbital, will proceed via a **C** mechanism. On the other hand, the same process in the quartet state nitrene complexes, having two half-filled Rh–Rh–N π* orbitals, is expected to proceed via the **S** mechanism. *Thus, the spin state of the nitrene intermediate is expected to play a significant role in determining the mechanism of C–H amination.* This is not a consequence of differing spin population, but orbital populations. Considering the electronic structure in Figure 6, one can easily see why the Co porphyrins use an **S** mechanism.

Armed with the aforementioned electronic structure-based prediction of the reactivity of the **2N_L** and **3N_L** nitrene species, we set out to investigate the mechanisms (energy and geometries of all transition states, intermediates and products) and controlling factors of intramolecular benzylic C–H bond amination in $NSO_3(CH_2)_3Ph$. Since the calculated energy difference between the doublet and quartet states of both starting **2N_L** and **3N_L** nitrene species is relatively small and is strongly dependent on the chemical compositions of these complexes, one may not clearly suggest which electronic state (doublet or quartet) of the **2N_L** and **3N_L** species is responsible in the amination reaction in experiments. In principle,

depending on the concentrations of exogenous L ligands in solution, any of these electronic states of both **2N_L** and **3N_L** nitrene species could be a catalytically important one. Therefore, we studied the mechanisms of the intramolecular benzylic C–H bond amination with the $NSO_3(CH_2)_3Ph$ ligand for all these species at their lowest energy doublet and quartet states. The calculated important intermediates, transition states and products of these reactions with their relative free energies are given in Figure 7. Representative transition state structures are given in Figure 8. More details of all these structures are given in the Supporting Materials.

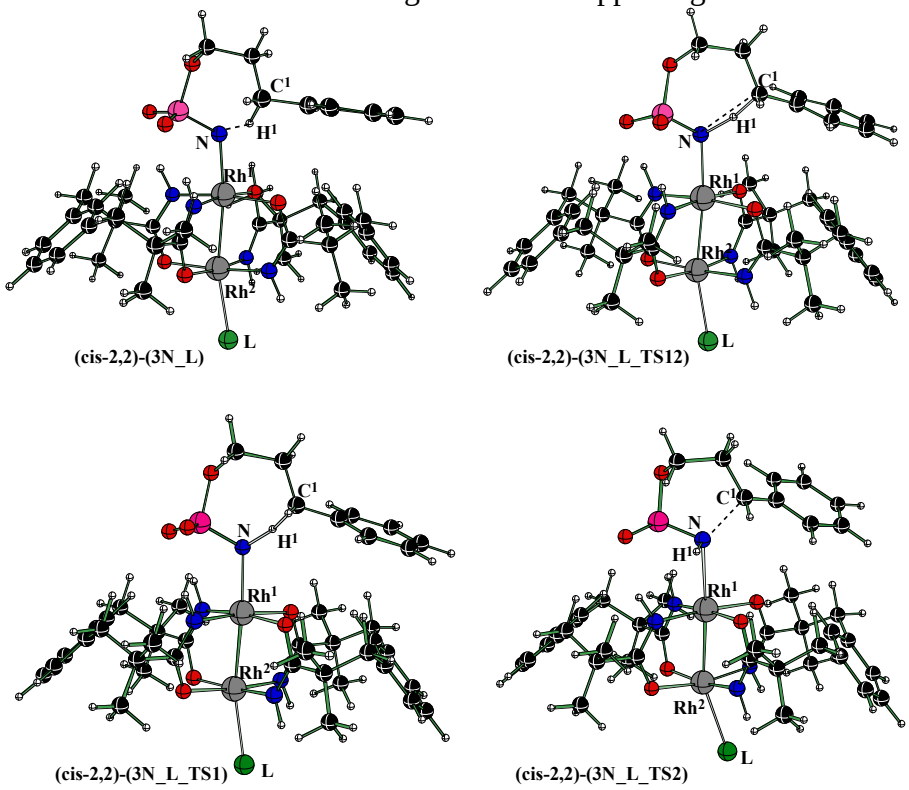

Figure 8. Calculated structures of the nitrene complex, and transition states **TS1, TS2** and **TS12**. The structures of L = Cl^- are shown here as an example. See Supporting Materials for similar structures for other species.

Intramolecular C–H Amination. The exact mechanism of C–H amination is expected to depend strongly on the spin state of the nitrene reactant. As seen in Figure 7, all doublet nitrene species uniformly undergo nearly barrierless (0.4 – 9.6 kJ/mol, at the transition state **TS12**), concerted insertion of the nitrene into the C^1–H^1 bond. On the other hand, the quartet nitrene species undergo stepwise C^1–H^1 functionalization via a mechanism involving: (1) H^1-atom abstraction with energy barriers of 3.8 – 42.3 kJ/mol, **TS1**, followed by (2) radical recombination, **TS2**. The recombination step is essentially barrierless for the **2N** species, but for **3N** is uphill from the intermediate **PROD-1** by 5.8 – 53.5 kJ/mol, due to the different occupancies of the π^* orbitals, depending strongly on the identity of L.

While it is tempting to assign the concerted pathway as the lowest-energy pathway and therefore the preferred pathway for catalysis, we must also keep in mind that in **3N_L** the quartet states are lower in energy, and spin crossover to the doublet surface would be necessary in order to access the fastest rates of the doublet potential energy surface (see Scheme 5).[74-75] However, we should also consider that formation of **3N** is most likely to take place on a doublet surface ($^2Rh_2$(II,III) + $^1PhINSO_3R$ → ^{2}**3N** + PhI). The main assumption underlying the proposed two-state reactivity for **3N** is that spin state crossover is fast compared to the other barriers involved in nitrene formation and C–H amination. Under this assumption, the energy barriers are necessarily steeper for the **3N_L** compounds than their **2N_L** analogs since the former must undergo a spin state change.

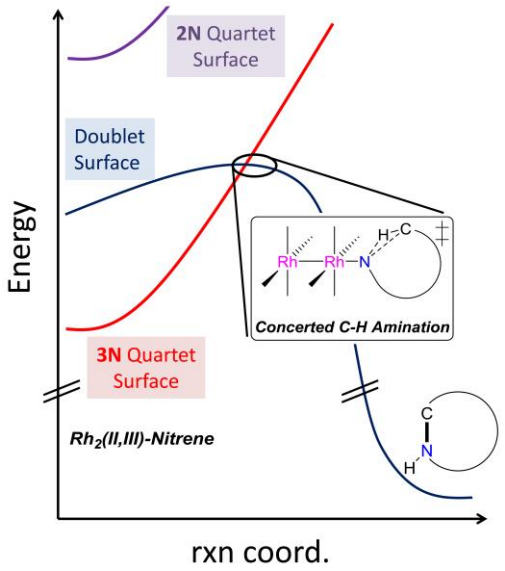

Scheme 5. Simplified reaction coordinate diagram for C–H amination by Rh_2(II,III) complexes.

Kinetic Isotope Effects. One way to assess the computed reaction pathways is comparison of the predicted and measured kinetic isotope effect (KIE) of the reactions. We have experimentally determined the KIE under identical conditions for compounds **2** and **3** (see Chart 3), which are 2.9 and 2.6, respectively. These are remarkably similar, especially considering that catalyst **2** is proposed to utilize both a Rh_2(II,III) and an Rh_2(II,II) mechanism. In comparison, the KIE for **1**, 1.9,[76-77] is somewhat smaller and may suggest that a Rh_2(II,III) pathway is not viable for **1**. Undoubtedly, the KIE must be a product of all of the potential mechanisms, and can even change over the course of a reaction if the nature of the active catalyst is changing, as is likely the case here. Given that KIEs of ~ 2 are established for concerted nitrene transfer reactions, whereas values of ~6 are associated with HAT steps, the experimental KIE values are more suggestive of a concerted intramolecular nitrene insertion mechanism.[78]

In agreement with this assessment, the calculated KIE values are 3.1, 2.3 and 2.8 for doublet state **2_N_L** with L = none, H_2O and Cl^-, respectively, while the corresponding values for the quartet surface are 6.3, 6.1 and 5.9. For the **3_N_L** catalysts (L =none, H_2O and Cl^-), the doublet KIE's are calculated to be 2.5, 1.8 and 2.1 and the quartet values are 5.9, 6.3 and 5.4. Thus, the calculated KIEs are significantly larger for the quartet state pathways than they are on the doublet state analogs. Moreover, the quartet values are too large compared to the experimental values. Thus, the doublet transition state appears to be the most important one for defining the C–H amination pathway despite the fact that the **3N_L** nitrene intermediates favor a quartet ground state. It is worth mentioning that since the exact identities of catalytic intermediates and active oxidant remain obscure at this time, we cannot hope to achieve better agreement between the experimental and computed KIE's.

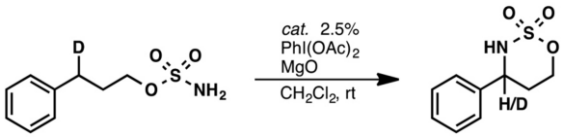

Chart 3. Reaction and conditions for experimental KIE measurement

3. Conclusions

From the above presented joint computational and experimental studies we may draw the following conclusions:

(a) Rh_2(II,III) tetracarboxylate complexes, $[Rh_2^{II,III}(O_2CCH_3)_4(L)_n]^+$ (**1_L**) (**L** = none, Cl^-, and H_2O), have a ^2E_u-derived ground electronic state with degenerate π*-orbitals and a $(\pi^*)^3$ valence electronic configuration; therefore, the electronic structure of these compounds cannot be adequately modeled at the DFT level. CASSCF calculations of the EPR *g* values are in good agreement with their experimental values.

(b) Unlike typical Rh_2(II,III) tetracarboxylates, $[Rh_2(esp)_2(L)_n]^{m+}$, **2_(L)$_n$**, and $[Rh_2(espn)_2(L)_n]^{m+}$, **3_(L)$_n$**, [where L = none with m=1, L = H_2O, n=1 or 2, with m=1, L = Cl^-, n=1, with m =0, and L = Cl^-, n=2, with m = –1] species have a $^2B_{1u}$-derived ground electronic state with a $(\delta^*)^1$ valence electronic configuration, as evidenced by EPR spectroscopy and Cl K-edge XAS. Importantly, this state is not a multi-reference state and, therefore, can be modeled well using DFT methods.

(c) Nitrene complexes **2N_L** and **3N_L** of $[Rh_2(esp)_2(L)_n]^{m+}$, **2_(L)$_n$**, and $[Rh_2(espn)_2(L)_n]^{m+}$, **3_(L)$_n$**, respectively, are proposed to be reactive intermediates in C–H amination. For **2N**, a complex multideterminental doublet state is predicted to be lowest in energy, whereas **3N** favors a high-spin quartet ground electronic state with a $(\delta^*)^1(\pi^*)^2$ valence electronic configuration. Binding π-donor axial ligands destabilizes the quartet state.

(d) The calculated energy barriers for stepwise C–H amination in the quartet state are found to be uniformly higher than for concerted C–H amination in the doublet state. While **2N** is able to access the doublet surface directly, **3N** must undergo a change in spin state first, which leads in effect to higher barriers to C–H amination by the latter species. Thus, the gain in catalyst robustness in changing from carboxylate to amidate equatorial ligands is counterbalanced by a loss in catalyst efficiency.

(e) Experimental KIE measurements yield values that are too low to be in agreement with a stepwise, C–H abstraction/radical recombination pathway and show better agreement with the mechanism outlined in Scheme 5.

4. Experimental Section

General Reagents and Methods. Catalysts **1** and **2** were prepared by published methods.[6, 40] All solvents were used as received without further purification unless otherwise noted. Electrochemical oxidation of **1** was performed according to a published protocol.[39]

Electron Paramagnetic Resonance. EPR data were acquired using a Varian Line X-band spectrometer equipped with a Varian E102 microwave bridge interfaced with a Linux system. An Oxford Instruments ESR-900 continuous-flow helium flow cryostat and an Oxford Instruments 3120 temperature controller were used to set and maintain the sample temperature. A Hewlett-Packard 432A power meter was used for microwave power calibration. Simulations were performed using EasySpin software.[79] The hyperfine fittings are based on line shape analysis.

X-Ray Absorption Spectroscopy. Cl K-edge XAS spectra were measured at SSRL beamline 4-3 under ring conditions of 3 GeV and 500 mA. Samples were ground to a fine powder and were spread to a vanishing thickness onto 38 μm low-S Mylar tape. All samples were measured in a He atmosphere at room temperature in fluorescence mode using a Lytle detector. The incident beam energy was calibrated by setting the energy of the first inflection point in the Cl K-edge spectrum of KCl to 2824.8 eV. Intensity was normalized with respect to the incident beam using a He-filled ion chamber upstream of the sample. Data represent an average of 6 scans measured from 2720 to 3150 eV. Data were processed with SIXPACK. Spectra were normalized by fitting a polynomial flattened to energies below 2840 eV to the data and normalizing the region above this energy to unity.

General Procedure for KIE experiments. 3-phenylpropyl-3-d sulfamate (105 mg, 0.48 mmol, 1.0 equiv) was combined with MgO (45mg, 1.11 mmol, 2.3 equiv), dirhodium catalyst (12 mmol, 0.025 equiv) and 3.0 mL of CH_2Cl_2. The resulting suspension was stirred for 5 min, after which time $PhI(OAc)_2$ (172 mg, 0.534 mmol, 1.1 equiv) was added in a single portion. The reaction flask was sealed and the mixture was stirred for 12 h. At the conclusion of this period, the suspension was filtered through a short pad of Celite, and the flask and filter cake were rinsed with 5–10 mL of CH_2Cl_2. The filtrate was concentrated under reduced pressure to a purple oil. Purification of this material by chromatography on silica gel (20% EtOAc in hexanes) afforded the desired product mixture as a white solid. The kinetic isotope effect value was determined by ^{13}C NMR analysis using the method of Wang and Adams.[80]

Computational Methods. Calculations of g-tensors, redox potentials, and multiconfigurational electronic structures were performed using the ORCA software package.[81] Potential energy surface calculations were performed by the Gaussian_09 suite of programs.[82] Orbitals were visualized using the MOLEKEL software program[83] or UCSF chimera software program.[84]

Calculation of EPR *g*-tensors of 1_L and 2L. EPR g-tensors of **1_L** and [*trans*-$Rh_2(esp)_2]^+$ was calculated on top of DFT optimized geometry according to the method described above. For **1_Cl2,** the geometry was obtained from the reported crystal structure of $((NH_2)_3C)_2[Rh_2(OAc)_4Cl_2]$ without further optimization. To calculate the g-tensors for all the complexes studied, B3LYP functional with scalar relativistically recontracted basis set of TZVP (SARC-TZVP)[85-86] was used. Scalar relativistic effects were accounted for in the Hamiltonian by the zeroth order regular approximation (ZORA) using the model potential of van Wullen.[87]

Ab initio multireference configuration interaction (MRCI) calculations of the molecular *g*-tensors for dirhodium tetraacetate complexes were performed on top of DFT optimized geometries, except for $[Rh_2(OAc)_4Cl_2]^-$ (*vide infra*). The DFT geometries were optimized using the BP86[88-89] functional with the SARC-def2-TZVPP basis set on Rh and the SARC-def2-SVP basis set on the rest of the atoms. Scalar relativistic effects were accounted for by ZORA. The evaluation of the Coulomb integrals were approximated by the resolution of identity (RI) approach.[90] Dispersion effects were treated with the D3[91] correction. The MRCI calculations were performed at the state-averaged complete active space self-consistent field (SA-CASSCF)[92] wavefunctions. Here, the MRCI approach was modeled by the multireference diference-dedicated configuration interaction theory with two degrees of freedom (MR-DDCI2).[93-94] To calculate the molecular *g*-tensors, first order perturbation on the converged MRDDCI2:CASSCF wavefunction using the electronic Zeeman Hamiltonian was performed. The effect of spin-orbit

coupling was introduced using the quasi-degenerate perturbation theory (QDPT)[95-96] with the spin-orbit mean field Hamiltonian (SOMF). In the SA-CASSCF calculations we used different active spaces to incorporate the effects of axial ligands. An active space of thirteen electrons in eight orbitals (13,8) was used for the axially-free $[Rh_2(OAc)_4]^+$ complex to include all metal d-orbitals except the two $d_x2_{-y}2$ orbitals which are highly antibonding with respect to the equatorial ligands. An active space of (17,10), which includes all spin-orbitals in (13,8) and four electrons in two σ orbitals from both H_2O ligands, was used for the bis(aquo) complex. An active space of (19,11), which includes all spin-orbitals in (13,8) and six electrons in three orbitals from the 3p orbitals of Cl^-, was used for the chloro complex. An active space of twenty-five electrons in fourteen orbitals (25,14), which includes all spin-orbitals in (13,8) and twelve electrons in six orbitals from the 3p orbitals of both Cl^-, was used for the dichloro complex.

CASSCF calculations on the nitrene complexes, **2N** and **3N**, were performed on truncated models, denoting 2N′ and 3N′, with the organic substituent on the nitrene replaced by a methyl group. A (19,12) active space was used. This active space includes (13,8) from both rhodium atoms and (7,4) from the nitrene, which are N 2s orbital and nitrene one σ and two π orbitals. The inclusion of N 2s orbital helps stabilize the convergence of the CASSCF calculations.

Calculation of the redox potentials of 2_L and 3_L. DFT prediction of redox potentials was performed using a slightly modified procedure following an established method.[56] Geometries were optimized in gas phase followed by single point energy calculations in CH_2Cl_2. Solvation were modeled by conductor-like screening model (COSMO). The Gibbs free energies of the redox half reaction in CH_2Cl_2 were calculated as follow:

$$\Delta G_{solv}^{abs,redox} = \Delta \mathrm{G}_{g}^{\mathrm{abs,redox}} + \Delta G_s^o(Red)$$

and the calculated Gibbs free energies were converted to absolute electron redox potential according to Nernst equation:

$$\Delta \mathrm{G}_{\mathrm{solv}}^{\mathrm{abs,redox}} = -FE_{calc}^{abs}$$

where *F* is the Faraday constant, 96,500 C mol^{-1}. The calculated absolute redox potentials of the half reaction were converted to standard potentials:

$$E_{calc}^o = E_{calc}^{abs} + E^{abs}(H_2/H^+)$$

where $E_{calc}^{abs}(H_2/H^+)$ is a literature value of –4.44 V.[97] The calculated standard potentials were converted to referenced potentials (*vs* Fc/Fc^+):

$$E_{calc}^{Fc} = E_{calc}^o - E^o(Fc/Fc^+)$$

where $E^o(Fc/Fc^+)$ is 0.46 V.[98]

Calculation of the C-H amination by 2N_L and 3N_L. Studies of potential energy surfaces of the C–H amination in **2N_L** and **3N_L** complexes, used the M06L density functional[99] in conjunction with the 6-31G** basis sets for C, H, N, O and S atoms[100] and

LANL08(f) basis sets (with their corresponding ECPs) for Rh atoms (referred to below as basis sets BS1).[101-103] All reported structures were fully optimized without any geometry constraints. Previously, it was reported that this computational method describes the energies and geometries of organometallic compounds well.[64-67] Frequency calculations were carried out to verify the nature of the located stationary points. Graphical analysis of the imaginary vibrational normal modes as well as the performed IRC calculations confirmed the nature of the located transition-states. Energetics of the reported structures were improved by performing single-point energy calculations at the M06L level of theory in conjunction with the 6-311+G(df,p) basis sets for C, H, O, N, S atoms[100] and LANL08(f) for the Rh-centers (referred to below as basis sets BS2). In these calculations we used the M06L/BS1 optimized geometries, respectively. The reported thermodynamic data were computed at the 298.15K temperature and 1atm pressure. Solvent effects in dichloromethane were included by means of the PCM method.[104] In these calculations the free energy of solvation was computed as:

$$\Delta\Delta G_{solv} = G_{solv,PCM} - E_{el}$$

where the final free energy in solution is obtained as:

$$G_{solv} = G_{gas} + \Delta\Delta G_{solv}$$

Acknowledgments. We thank the Center for Selective C-H Functionalization supported by National Science Foundation (CHE-1205646). J.F.B. additionally thanks the DOE (DE-FG02-10ER16204). K.M.L. acknowledges NSF CHE-1454455 for support. The authors gratefully acknowledge NSF MRI-R2 grant (CHE-0958205) and the use of the resources of the Cherry Emerson Center for Scientific Computation. The computational and EPR facilities at UW–Madison are supported by grants from the National Science Foundation (CHE-0840494 and CHE-0741901, respectively). The UCSF Chimera package is developed by the Resource for Biocomputing, Visualization, and Informatics at the University of California, San Francisco (supported by NIGMS P41-GM103311).

Supporting Information Available. Figures S1 and S2, and Tables S1 – S3. This information is available free of charge on the Internet via the ACS Publications website.

References.

1. Davies, H. M. L.; Manning, J. R., *Nature* **2008,** *451*, 417-424.
2. Zalatan, D. N.; Du Bois, J., In *Topics in Current Chemistry*, Yu, J.-Q.; Shi, Z., Eds. Springer-Verlag: Berlin, 2010; Vol. 292, pp 347-378.
3. Du Bois, J., *Org. Proc. Res. Dev.* **2011,** *15*, 758-762.
4. Roizen, J. L.; Harvey, M. E.; Du Bois, J., *Acc. Chem. Res.* **2012,** *45*, 911-922.
5. Kornecki, K. P.; Berry, J. F.; Powers, D. C.; Ritter, T., In *Progress in Inorganic Chemistry*, Karlin, K. D., Ed. 2014; Vol. 58, pp 225-302.
6. Espino, C. G.; Fiori, K. W.; Kim, M.; Du Bois, J., *J. Am. Chem. Soc.* **2004,** *126*, 15378-15379.
7. Cui, Y.; He, C., *Angew. Chem. Int. Ed.* **2004,** *43*, 4210-4212.
8. Li, Z. G.; Capretto, D. A.; Rahaman, R.; He, C. A., *Angew. Chem. Int. Ed.* **2007,** *46*, 5184-5186.
9. Beltran, A.; Lescot, C.; Diaz-Requejo, M. M.; Perez, P. J.; Dauban, P., *Tetrahedron* **2013,** *69*, 4488-4492.
10. Rigoli, J. W.; Weatherly, C. D.; Alderson, J. M.; Vo, B. T.; Schomaker, J. M., *J. Am. Chem. Soc.* **2013,** *135*, 17238-17241.
11. Scamp, R. J.; Rigoli, J. W.; Schomaker, J. M., *Pure Appl. Chem.* **2014,** *86*, 381-393.
12. Breslow, R.; Gellman, S. H., *J. Am. Chem. Soc.* **1983,** *105*, 6728-6729.
13. Mahy, J. P.; Bedi, G.; Battioni, P.; Mansuy, D., *New J. Chem.* **1989,** *13*, 651-657.
14. Liu, Y. G.; Che, C. M., *Chem. Eur. J.* **2010,** *16*, 10494-10501.
15. Liu, Y. G.; Wei, J. H.; Che, C. M., *Chem. Commun.* **2010,** *46*, 6926-6928.
16. Paradine, S. M.; White, M. C., *J. Am. Chem. Soc.* **2012,** *134*, 2036-2039.
17. Liu, Y. G.; Guan, X. G.; Wong, E. L. M.; Liu, P.; Huang, J. S.; Che, C. M., *J. Am. Chem. Soc.* **2013,** *135*, 7194-7204.
18. Yu, X. Q.; Huang, J. S.; Zhou, X. G.; Che, C. M., *Org. Lett.* **2000,** *2*, 2233-2236.
19. Wang, H. Y.; Li, Y. X.; Wang, Z. M.; Lou, J.; Xiao, Y. L.; Qiu, G. F.; Hu, X. M.; Altenbach, H. J.; Liu, P., *RSC Adv.* **2014,** *4*, 25287-25290.
20. Paradine, S. M.; Griffin, J. R.; Zhao, J. P.; Petronico, A. L.; Miller, S. M.; White, M. C., *Nature Chem.* **2015,** *7*, 987-994.
21. Liang, J. L.; Yuan, S. X.; Huang, J. S.; Che, C. M., *J. Org. Chem.* **2004,** *69*, 3610-3619.
22. Milczek, E.; Boudet, N.; Blakey, S., *Angew. Chem. Int. Ed.* **2008,** *47*, 6825-6828.
23. Au, S. M.; Huang, J. S.; Yu, W. Y.; Fung, W. H.; Che, C. M., *J. Am. Chem. Soc.* **1999,** *121*, 9120-9132.
24. Diaz-Requejo, M. M.; Belderrain, T. R.; Nicasio, M. C.; Trofimenko, S.; Perez, P. J., *J. Am. Chem. Soc.* **2003,** *125*, 12078-12079.
25. Pelletier, G.; Powell, D. A., *Org. Lett.* **2006,** *8*, 6031-6034.
26. Powell, D. A.; Fan, H., *J. Org. Chem.* **2010,** *75*, 2726-2729.
27. Gephart, R. T.; Warren, T. H., *Organometallics* **2012,** *31*, 7728-7752.
28. Bagchi, V.; Paraskevopoulou, P.; Das, P.; Chi, L. Y.; Wang, Q. W.; Choudhury, A.; Mathieson, J. S.; Cronin, L.; Pardue, D. B.; Cundari, T. R.; Mitrikas, G.; Sanakis, Y.; Stavropoulos, P., *J. Am. Chem. Soc.* **2014,** *136*, 11362-11381.
29. Caballero, A.; Diaz-Requejo, M. M.; Belderrain, T. R.; Nicasio, M. C.; Trofimenko, S.; Perez, P. J., *J. Am. Chem. Soc.* **2003,** *125*, 1446-1447.
30. Fructos, M. R.; Trofimenko, S.; Diaz-Requejo, M. M.; Perez, P. J., *J. Am. Chem. Soc.* **2006,** *128*, 11784-11791.

31. Huang, G. H.; Li, J. M.; Huang, J. J.; Lin, J. D.; Chuang, G. J., *Chem. Eur. J.* **2014,** *20*, 5240-5243.
32. Cui, X.; Xu, X.; Jin, L. M.; Wojtas, L.; Zhang, X. P., *Chem. Sci.* **2015,** *6*, 1219-1224.
33. Lu, H. J.; Li, C. Q.; Jiang, H. L.; Lizardi, C. L.; Zhang, X. P., *Angew. Chem. Int. Ed.* **2014,** *53*, 7028-7032.
34. Lu, H. J.; Hu, Y.; Jiang, H. L.; Wojtas, L.; Zhang, X. P., *Org. Lett.* **2012,** *14*, 5158-5161.
35. Fiori, K. W.; Du Bois, J., *J. Am. Chem. Soc.* **2007,** *129*, 562-568.
36. Davies, H. M. L.; Morton, D., *Chem. Soc. Rev.* **2011,** *40*, 1857-1869.
37. Zalatan, D. N.; Du Bois, J., *J. Am. Chem. Soc.* **2009,** *131*, 7558-+.
38. Perry, R. H.; Cahill, T. J., III; Roizen, J. L.; Du Bois, J.; Zare, R. N., *Proc. Nat. Acad. Sci. U. S. A.* **2012,** *109*, 18295-18299.
39. Kornecki, K. P.; Berry, J. F., *Chem. Eur. J.* **2011,** *17*, 5827-5832.
40. Kornecki, K. P.; Berry, J. F., *Chem. Commun.* **2012,** *48*, 12097-12099.
41. Doyle, M. P., *J. Org. Chem.* **2006,** *71*, 9253-9260.
42. Norman, J. G.; Renzoni, G. E.; Case, D. A., *J. Am. Chem. Soc.* **1979,** *101*, 5256-5267.
43. Cotton, F. A.; Murillo, C. A.; Walton, R. A., In *Multiple Bonds Between Metal Atoms*, 3rd ed.; Springer Science and Business Media, Inc.: New York, 2005.
44. Lichtenberger, D. L.; Pollard, J. R.; Lynn, M. A.; Cotton, F. A.; Feng, X. J., *J. Am. Chem. Soc.* **2000,** *122*, 3182-3190.
45. McNaughton, R. L.; Roemelt, M.; Chin, J. M.; Schrock, R. R.; Neese, F.; Hoffman, B. M., *J. Am. Chem. Soc.* **2010,** *132*, 8645-8656.
46. Kawamura, T.; Fukamachi, K.; Sowa, T.; Hayashida, S.; Yonezawa, T., *J. Am. Chem. Soc.* **1981,** *103*, 364-369.
47. Kawamura, T.; Katayama, H.; Yamabe, T., *Chem. Phys. Lett.* **1986,** *130*, 20-23.
48. Kawamura, T.; Katayama, H.; Nishikawa, H.; Yamabe, T., *J. Am. Chem. Soc.* **1989,** *111*, 8156-8160.
49. Kawamura, T.; Maeda, M.; Miyamoto, M.; Usami, H.; Imaeda, K.; Ebihara, M., *J. Am. Chem. Soc.* **1998,** *120*, 8136-8142.
50. Chavan, M. Y.; Zhu, T. P.; Lin, X. Q.; Ahsan, M. Q.; Bear, J. L.; Kadish, K. M., *Inorg. Chem.* **1984,** *23*, 4538-4545.
51. Schafer, A.; Horn, H.; Ahlrichs, R., *J. Chem. Phys.* **1992,** *97*, 2571-2577.
52. Vosko, S. H.; Wilk, L.; Nusair, M., *Can. J. Phys.* **1980,** *58*, 1200-1211.
53. Lee, C. T.; Yang, W. T.; Parr, R. G., *Phys. Rev. B* **1988,** *37*, 785-789.
54. Becke, A. D., *J. Chem. Phys.* **1993,** *98*, 1372-1377.
55. Stephens, P. J.; Devlin, F. J.; Chabalowski, C. F.; Frisch, M. J., *J. Phys. Chem.* **1994,** *98*, 11623-11627.
56. Roy, L. E.; Jakubikova, E.; Guthrie, M. G.; Batista, E. R., *J. Phys. Chem. A* **2009,** *113*, 6745-6750.
57. For **1**, a $^2B_{1u}$ state was initially obtained, but the ~2 kcal/mol lower energy ^2E_u state could be converged by rotation of the orbitals.
58. Bersuker, I. B., *J. Comp. Chem.* **1997,** *18*, 260-267.
59. Warzecha, E.; Berto, T. C.; Berry, J. F., *Inorg. Chem.* **2015,** *54*, 8817-8824.
60. Berry, J. F., *Dalton Trans.* **2012,** *41*, 700-713.
61. Kornecki, K. P.; Briones, J. F.; Boyarskikh, V.; Fullilove, F.; Autschbach, J.; Schrote, K. E.; Lancaster, K. M.; Davies, H. M. L.; Berry, J. F., *Science* **2013,** *342*, 351-354.
62. Pap, J. S.; George, S. D.; Berry, J. F., *Angew. Chem. Int. Ed.* **2008,** *47*, 10102-10105.

63. Sperger, T.; Sanhueza, I. A.; Kalvet, I.; Schoenebeck, F., *Chem. Rev.* **2015**, *115*, 9532-9586.
64. Harvey, M. E.; Musaev, D. G.; Du Bois, J., *J. Am. Chem. Soc.* **2011,** *133*, 17207-17216.
65. Qin, C.; Boyarskikh, V.; Hansen, J. H.; Hardcastle, K. I.; Musaev, D. G.; Davies, H. M. L., *J. Am. Chem. Soc.* **2011,** *133*, 19198-19204.
66. Li, Z.; Boyarskikh, V.; Hansen, J. H.; Autschbach, J.; Musaev, D. G.; Davies, H. M. L., *J. Am. Chem. Soc.* **2012,** *134*, 15497-15504.
67. Wang, H.; Guptill, D. M.; Varela-Alvarez, A.; Musaev, D. G.; Davies, H. M. L., *Chem. Sci.* **2013,** *4*, 2844-2850.
68. Berry, J. F., *Comments Inorg. Chem.* **2009,** *30*, 28-66.
69. Brown, T. R.; Dolinar, B. S.; Hillard, E. A.; Clerac, R.; Berry, J. F., *Inorg. Chem.* **2015,** *54*, 8571-8589.
70. Goswami, M.; Lyaskovskyy, V.; Domingos, S. R.; Buma, W. J.; Woutersen, S.; Troeppner, O.; Ivanovic-Burmazovic, I.; Lu, H. J.; Cui, X.; Zhang, X. P.; Reijerse, E. J.; DeBeer, S.; van Schooneveld, M. M.; Pfaff, F. F.; Ray, K.; de Bruin, B., *J. Am. Chem. Soc.* **2015,** *137*, 5468-5479.
71. Truxillo, L. A.; Davis, D. G., *Anal. Chem.* **1975,** *47*, 2260-2267.
72. Lyaskovskyy, V.; Suarez, A. I. O.; Lu, H. J.; Jiang, H. L.; Zhang, X. P.; de Bruin, B., *J. Am. Chem. Soc.* **2011,** *133*, 12264-12273.
73. Saouma, C. T.; Mayer, J. M., *Chem. Sci.* **2014,** *5*, 21-31.
74. Schroder, D.; Shaik, S.; Schwarz, H., *Acc. Chem. Res.* **2000,** *33*, 139-145.
75. Harvey, J. N.; Poli, R.; Smith, K. M., *Coord. Chem. Rev.* **2003,** *238*, 347-361.
76. Fiori, K. W.; Espino, C. G.; Brodsky, B. H.; Du Bois, J., *Tetrahedron* **2009,** *65*, 3042-3051.
77. We note that this KIE increases to 2.6 when one uses a longer delay time on the ^{13}C NMR acquisition, as described in Ref. 64. Thus, we cannot completely rule out a Rh_2(II,III) pathway for $Rh_2(OAc)_4$.
78. Collet, F.; Lescot, C.; Liang, C.; Dauban, P., *Dalton Trans.* **2010,** *39*, 10401-10413.
79. Stoll, S.; Schweiger, A., *J. Magn. Res.* **2006,** *178*, 42-55.
80. Wang, P.; Adams, J., *J. Am. Chem. Soc.* **1994,** *116*, 3296-3305.
81. Neese, F., *Wiley Interdisciplinary Reviews-Computational Molecular Science* **2012,** *2*, 73-78.
82. Frisch, M. J.; Trucks, G. W.; Schlegel, H. B.; Scuseria, G. E.; Robb, M. A.; Cheeseman, J. R.; Scalmani, G.; Barone, V.; Mennucci, B.; Petersson, G. A.; Nakatsuji, H.; Caricato, M.; Li, X.; Hratchian, H. P.; Izmaylov, A. F.; Bloino, J.; Zheng, G.; Sonnenberg, J. L.; Hada, M.; Ehara, M.; Toyota, K.; Fukuda, R.; Hasegawa, J.; Ishida, M.; Nakajima, T.; Honda, Y.; Kitao, O.; Nakai, H.; Vreven, T.; Montgomery, Jr., J. A.; Peralta, J. E.; Ogliaro, F.; Bearpark, M.; Heyd, J. J.; Brothers, E.; Kudin, K. N.; Staroverov, V. N.; Kobayashi, R.; Normand, J.; Raghavachari, K.; Rendell, A.; Burant, J. C.; Iyengar, S. S.; Tomasi, J.; Cossi, M.; Rega, N.; Millam, J. M.; Klene, M.; Knox, J. E.; Cross, J. B.; Bakken, V.; Adamo, C.; Jaramillo, J.; Gomperts, R.; Stratmann, R. E.; Yazyev, O.; Austin, A. J.; Cammi, R.; Pomelli, C.; Ochterski, J. W.; Martin, R. L.; Morokuma, K.; Zakrzewski, V. G.; Voth, G. A.; Salvador, P.; Dannenberg, J. J.; Dapprich, S.; Daniels, A. D.; Farkas, Ö.; Foresman, J. B.; Ortiz, J. V.; Cioslowski, J.; Fox, D. J. 09, Revision D01;Gaussian, Inc.: Wallingford, CT, 2009.
83. Flükiger, P.; Lüthi, H. P.; Portmann, S.; Weber, J. *MOLEKEL*, 4.0; Swiss Center for Scientific Computing: Manno, Switzerland, 2000.

84. Pettersen, E. F.; Goddard, T. D.; Huang, C. C.; Couch, G. S.; Greenblatt, D. M.; Meng, E. C.; Ferrin, T. E., *J. Comp. Chem.* **2004,** *25*, 1605-1612.
85. Pantazis, D. A.; Chen, X.-Y.; Landis, C. R.; Neese, F., *J. Chem. Theory Comp.* **2008,** *4*, 908-919.
86. Weigend, F.; Ahlrichs, R., *Phys. Chem. Chem. Phys.* **2005,** *7*, 3297-3305.
87. van Wullen, C., *J. Chem. Phys.* **1998,** *109*, 392-399.
88. Perdew, J. P., *Phys. Rev. B* **1986,** *33*, 8822-8824.
89. Becke, A. D., *Phys. Rev. A* **1988,** *38*, 3098-3100.
90. Weigend, F., *Phys. Chem. Chem. Phys.* **2006,** *8*, 1057-1065.
91. Grimme, S.; Antony, J.; Ehrlich, S.; Krieg, H., *J. Chem. Phys.* **2010,** *132*.
92. Roos, B. O.; Taylor, P. R.; Siegbahn, P. E. M., *Chem. Phys.* **1980,** *48*, 157-173.
93. Miralles, J.; Daudey, J. P.; Caballol, R., *Chem. Phys. Lett.* **1992,** *198*, 555-562.
94. Miralles, J.; Castell, O.; Caballol, R.; Malrieu, J. P., *Chem. Phys.* **1993,** *172*, 33-43.
95. Ganyushin, D.; Neese, F., *J. Chem. Phys.* **2006,** *125*.
96. Neese, F.; Petrenko, T.; Ganyushin, D.; Olbrich, G., *Coord. Chem. Rev.* **2007,** *251*, 288-327.
97. Trasatti, S., *Pure Appl. Chem.* **1986,** *58*, 955-966.
98. Connelly, N. G.; Geiger, W. E., *Chem. Rev.* **1996,** *96*, 877-910.
99. Zhao, Y.; Truhlar, D. G., *J. Chem. Phys.* **2006,** *125*.
100. Hehre, W. J.; Radom, L.; Schleyer, P. v. R.; Pople, J. A., *Ab initio Molecular Orbital Theory*. John Wiley & Sons: New York, 1986.
101. Hay, P. J.; Wadt, W. R., *J. Chem. Phys.* **1985,** *82*, 299-310.
102. Roy, L. E.; Hay, P. J.; Martin, R. L., *J. Chem. Theory Comp.* **2008,** *4*, 1029-1031.
103. Ehlers, A. W.; Bohme, M.; Dapprich, S.; Gobbi, A.; Hollwarth, A.; Jonas, V.; Kohler, K. F.; Stegmann, R.; Veldkamp, A.; Frenking, G., *Chem. Phys. Lett.* **1993,** *208*, 111-114.
104. Tomasi, J.; Mennucci, B.; Cammi, R., *Chem. Rev.* **2005,** *105*, 2999-3093.
105. Miskowski, V. M.; Dallinger, R. F.; Christoph, G. G.; Morris, D. E.; Spies, G. H.; Woodruff, W. H., *Inorg. Chem.* **1987,** *26*, 2127-2132.

Table 1. Calculated and experimentally measured EPR parameters of the $[Rh_2(OAc)_4(L)_n]^{m+}$, **1_L**, species (where L = none, H_2O and Cl^-).

Species	g_1	g_2	g_3	Methods
$[Rh_2(OAc)_4]^+$	7.36	2.61	2.04	RI-B3LYP
	4.00	0.05	0.05	MR-DDCI2:SA-CASSCF(13e/8o)
$[Rh_2(OAc)_4(H_2O)_2]^+$	3.61	1.50	1.50	Experiment[48]
	3.41	2.32	2.07	RI-B3LYP
	3.83	0.87	0.87	MR-DDCI2:SA-CASSCF(17e/10o)
$Rh_2(OAc)_4Cl$	27.4	2.43	2.13	RI-B3LYP
	3.99	0.18	0.18	MR-DDCI2:SA-CASSCF(19e/11o)
$[Rh_2(OAc)_4(Cl)_2]^{-}$ [a)]	4.00	0.60	0.60	Experiment[48]
	18.5	2.77	2.14	RI-B3LYP
	4.01	0.01	0.01	MR-DDCI2:SA-CASSCF(25e/14o)
$[Rh_2(esp)_2]^-$	2.14	2.14	1.93	Experiment (this work)
	2.25	2.25	1.89	Experiment (this work)
	2.24	2.11	2.06	RI-B3LYP

[a)] No crystal structure of $[Rh_2(OAc)_4(Cl)_2]^-$ was available, so the geometry was optimized using coordinates from the structure of $[Rh_2(OAc)_4Cl_2]^{2-}$.[105]

Table 2. Leading configurations in the SA-CASSCF wavefunctions of $[Rh_2(OAc)_4(L)_n]^{m+}$, **1_L**, species (where L = none, H_2O and Cl^-). [a]

Compound	Active Space	CSFs[b]	Weight (in %)
$[Rh_2(OAc)_4]^+$	(13,8)	$\delta^2\delta^{*2}\pi_1^2\pi_2^2\sigma^2\pi^*_1{}^2\pi^*_2{}^1\sigma^{*0}$	43.3
		$\delta^2\delta^{*2}\pi_1^2\pi_2^2\sigma^2\pi^*_1{}^1\pi^*_2{}^2\sigma^{*0}$	43.3
$[Rh_2(OAc)_4(H_2O)_2]^+$	(17,10)	$\pi^*_{2,+}{}^2\sigma^*_+{}^2\delta^2\delta^{*2}\pi_1^2\pi_2^2\sigma^2\pi^*_1{}^2\pi^*_{2,-}{}^1\sigma^*_-{}^0$	43.5
		$\pi^*_{2,+}{}^2\sigma^*_+{}^2\delta^2\delta^{*2}\pi_1^2\pi_2^2\sigma^2\pi^*_1{}^1\pi^*_{2,-}{}^2\sigma^*_-{}^0$	43.5
		$\pi^*_{2,+}{}^2\sigma^*_+{}^2\delta^2\delta^{*2}\pi_1^u\pi_2^2\sigma^d\pi^*_1{}^2\pi^*_{2,-}{}^2\sigma^*_-{}^u$	4.6
		$\pi^*_{2,+}{}^2\sigma^*_+{}^2\delta^2\delta^{*2}\pi_1^2\pi_2^u\sigma^d\pi^*_1{}^2\pi^*_{2,-}{}^2\sigma^*_-{}^u$	4.6
$Rh_2(OAc)_4Cl$	(19,11)	$\delta^2\delta^{*2}\pi_1^2\pi_2^2\pi_{1,nb}{}^2\pi_{2,nb}{}^2\sigma^2\sigma_{nb}{}^2\pi^*_1{}^2\pi^*_2{}^1\sigma^{*0}$	41.9
		$\delta^2\delta^{*2}\pi_1^2\pi_2^2\pi_{1,nb}{}^2\pi_{2,nb}{}^2\sigma^2\sigma_{nb}{}^2\pi^*_1{}^1\pi^*_2{}^2\sigma^{*0}$	41.9
		$\delta^2\delta^{*2}\pi_1^2\pi_2^2\pi_{1,nb}{}^2\pi_{2,nb}{}^2\sigma^2\sigma_{nb}{}^0\pi^*_1{}^2\pi^*_2{}^1\sigma^{*2}$	4.2
		$\delta^2\delta^{*2}\pi_1^2\pi_2^2\pi_{1,nb}{}^2\pi_{2,nb}{}^2\sigma^2\sigma_{nb}{}^0\pi^*_1{}^1\pi^*_2{}^2\sigma^{*2}$	4.2
$[Rh_2(OAc)_4Cl_2]^{-c}$	(25,14)	$\pi_{1,+}{}^2\pi_{2,+}{}^2\pi^*_{1,+}{}^2\pi^*_{2,+}{}^2\sigma_+{}^2\delta^2\delta^{*2}\sigma^*_+{}^2\pi_{1,-}{}^2\pi_{2,-}{}^2\sigma_-{}^2\pi^*_{1,-}{}^2\pi^*_{2,-}{}^1\sigma^*_-{}^0$	43.2
		$\pi_{1,+}{}^2\pi_{2,+}{}^2\pi^*_{1,+}{}^2\pi^*_{2,+}{}^2\sigma_+{}^2\delta^2\delta^{*2}\sigma^*_+{}^2\pi_{1,-}{}^2\pi_{2,-}{}^2\sigma_-{}^2\pi^*_{1,-}{}^1\pi^*_{2,-}{}^2\sigma^*_-{}^0$	42.8
		$\pi_{1,+}{}^2\pi_{2,+}{}^2\pi^*_{1,+}{}^2\pi^*_{2,+}{}^2\sigma_+{}^2\delta^2\delta^{*2}\sigma^*_+{}^2\pi_{1,-}{}^u\pi_{2,-}{}^2\sigma_-{}^d\pi^*_{1,-}{}^2\pi^*_{2,-}{}^1\sigma^*_-{}^u$	5.0
		$\pi_{1,+}{}^2\pi_{2,+}{}^2\pi^*_{1,+}{}^2\pi^*_{2,+}{}^2\sigma_+{}^2\delta^2\delta^{*2}\sigma^*_+{}^2\pi_{1,-}{}^0\pi_{2,-}{}^u\sigma_-{}^d\pi^*_{1,-}{}^2\pi^*_{2,-}{}^1\sigma^*_-{}^u$	5.0

[a]configurations with weight > 3% are reported. [b]CSFs = configuration state functions. All orbital symbols have their normal meaning; nb = non-bonding, + and – refer to in-phase and out-of-phase contributions of the equatorial ligands. [c]geometry for the single point calculation was obtained without further optimization from the crystal structure of $[(NH_2)_3C]_2[Rh_2(OAc)_4Cl_2]$.[105]

Table 3. Calculated and experimentally available important geometry parameters (distances in Å, and angles in deg.) of the $[Rh_2(esp)_2L]^+$, **2_L**, species (where L = none, H_2O and Cl^-).

Species	**Rh-Rh**	**Rh-L**	**Rh-O_{av}**	**Rh-Rh-L**
		Calculated: *This work*		
$[Rh_2(esp)_2]^+$	2.362	---	2.041	---
$[Rh_2(esp)_2(H_2O)]^+$	2.378	2.253	2.043	178.9
$Rh_2(esp)_2Cl$	2.394	2.361	2.065	180.0
		Experiment[39]		
$[Rh_2(esp)_2(Cl)_2]^-$	2.360(1)	2.475(1)	2.023(1)	174.4(1)

Table 4. Calculated and experimentally available important geometry parameters (distances in Å) of the (*cis*-2,2) and (4,0) isomers of $[Rh_2(espn)_2L]^+$, **3_L**, species (where L = none, H_2O and Cl^-), at their lower-lying doublet (S=1/2) and quartet (S=3/2) electronic states.

Species	Rh–Rh	Rh–L_{ax}	Rh–N_{eq}	Rh–O_{eq}	S
		Calculated: *This work*			
(*cis*-2,2)-$[Rh_2(espn)_2]^+$	2.40	---	2.02	2.05	1/2
	2.47	---	2.03	2.06	3/2
(*cis*-2,2)-$[Rh_2(espn)_2(H_2O)]^+$	2.41	2.28	2.02	2.06	1/2
	2.48	2.48	2.03	2.08	3/2
(*cis*-2,2)-$[Rh_2(espn)_2Cl]$	2.46	2.42	2.01	2.08	1/2
	2.54	2.62	2.02	2.08	3/2
		Experiment[40]			
(*cis*-2,2)-$[Rh_2(espn)_2Cl]_n$	2.4155(9)	2.617(2)	1.970(6)	2.033(5)	1/2
		Calculated: *This work*			
(4,0)-$[Rh_2(espn)_2]^+$	2.40	---	2.05	2.03	1/2
	2.47	---	2.05	2.03	3/2
(4,0)-$[Rh_2(espn)_2(H_2O)]^+$	2.41	2.34	2.05	2.03	1/2
	2.50	2.43	2.05	2.05	3/2
(4,0)-$[Rh_2(espn)_2Cl]$	2.44	2.44	2.04	2.04	1/2
	2.51	2.55	2.07	2.05	3/2
		Experiment[40]			
(4,0)-$[Rh_2(espn)_2Cl]$	2.4136(4)	2.6165(9)	2.003(3)	1.998(2)	1/2

Table 5. Calculated important geometry parameters (distances in Å, and angles in deg.) of the $\{Rh_2(esp)_2[NSO_3(CH_2)_3Ph](L)\}^+$, **2N_L,** species (where L = none, H_2O and Cl^-) at their doublet (S=1/2) and quartet (S=3/2) electronic states.

Species	S	Rh–Rh	Rh–N	Rh–L	Rh–Rh–L	Rh–Rh–N	Rh–N–S
2N	1/2	2.40	1.92	---	---	176	122
	3/2	2.42	1.95	---	---	172	125
2N_H_2O	1/2	2.39	1.93	2.31	167	170	129
	3/2	2.42	2.00	2.35	174	170	126
2N_Cl	1/2	2.44	1.93	2.34	165	161	126
	3/2	2.46	2.03	2.40	172	169	124

Table 6. Calculated important geometry parameters (distances in Å, and angles in deg.) of the $\{Rh_2(espn)_2[NSO_3(CH_2)_3Ph](L)\}^+$, **3_L**, species (where L = none, H_2O and Cl^-), at their doublet (S=1/2) and quartet (S=3/2) electronic states.

Species	S	Rh–Rh	Rh–N_{ax}	Rh–L_{ax}	Rh–N_{eq}	Rh–O_{eq}	Rh–Rh–L	Rh–Rh–N	Rh–N–S
(*cis*-2,2)-**3N**	1/2	2.46	1.94	---	2.02	2.08	---	174	119
	3/2	2.45	1.94	---	2.02	2.09	---	173	119
(*cis*-2,2)-**3N_H_2O**	1/2	2.44	1.99	2.39	2.03	2.07	174	171	129
	3/2	2.44	1.98	2.39	2.03	2.07	175	171	127
(*cis*-2,2)-**3N_Cl**	1/2	2.48	2.04	2.45	2.02	2.08	167	172	123
	3/2	2.48	2.03	2.46	2.02	2.09	166	172	123
(4,0)-**3N**	1/2	2.48	1.92	---	2.04	2.07	---	176	117
	3/2	2.43	1.96	---	2.05	2.02	---	176	127
(4,0)-**3N_H_2O**	1/2	2.44	2.00	2.34	2.06	2.03	174	172	128
	3/2	2.44	2.00	2.34	2.06	2.03	175	171	126
(4,0)-**3N_Cl**	1/2	2.48	2.04	2.45	2.02	2.09	166	172	123
	3/2	2.47	2.03	2.47	2.03	2.06	174	170	126

Table 7. Leading configurations from CASSCF calculations on **2N′** and **3N′** in doublet and quartet states.

Complex	S	Active space	CSFs[a]	weights
2N′	1/2	(19,12)	$(\pi''_{nb})^2(\sigma_{nb})^2(\delta^*)^2(\pi'^*)^1(\pi''^*)^0(\sigma^*)^0$	46.5%
			$(\pi''_{nb})^2(\sigma_{nb})^2(\delta^*)^0(\pi'^*)^1(\pi''^*)^2(\sigma^*)^0$	26.3%
			$(\pi''_{nb})^2(\sigma_{nb})^2(\delta^*)^1(\pi'^*)^1(\pi''^*)^1(\sigma^*)^0$	16.7%
2N′	3/2	(19,12)	$(\pi''_{nb})^2(\sigma_{nb})^2(\delta^*)^1(\pi'^*)^1(\pi''^*)^1(\sigma^*)^0$	90.5%
3N′	1/2	(19,12)	$(\pi''_{nb})^2(\sigma_{nb})^2(\delta^*)^1(\pi'^*)^2(\pi''^*)^0(\sigma^*)^0$	71.5%
			$(\pi''_{nb})^0(\sigma_{nb})^2(\delta^*)^1(\pi'^*)^2(\pi''^*)^2(\sigma^*)^0$	14.9%
			$(\pi''_{nb})^1(\sigma_{nb})^2(\delta^*)^1(\pi'^*)^2(\pi''^*)^1(\sigma^*)^0$	3.21%
3N′	3/2	(19,12)	$(\pi''_{nb})^2(\sigma_{nb})^2(\delta^*)^1(\pi'^*)^1(\pi''^*)^1(\sigma^*)^0$	83.5%

[a]CSFs = configuration state functions. All CSFs have six further doubly filled active orbitals, which are highly mixed.

Table 8. Unpaired Spin populations within the Rh–Rh–N unit in **2N′** and **3N′**, derived from the CASSCF wavefunctions.

Complex	S	Mulliken Spin Population[a]		
		N	Rh_m[b]	Rh_d[b]
2N′	1/2	1.05	0.12	–0.23
2N′	3/2	1.68	0.08	1.07
3N′	1/2	–0.07	0.02	0.93
3N′	3/2	1.09	0.55	1.12

[a]Residual spin populations are located primarily on the SO_3CH_3 group.
[b]Rh_m = middle rhodium; Rh_d = distal rhodium.

Table of Contents Figure: